Article

Cell Reports

Mesenchymal Cancer Cell-Stroma Crosstalk Promotes Niche Activation, Epithelial Reversion, and Metastatic Colonization

Graphical Abstract

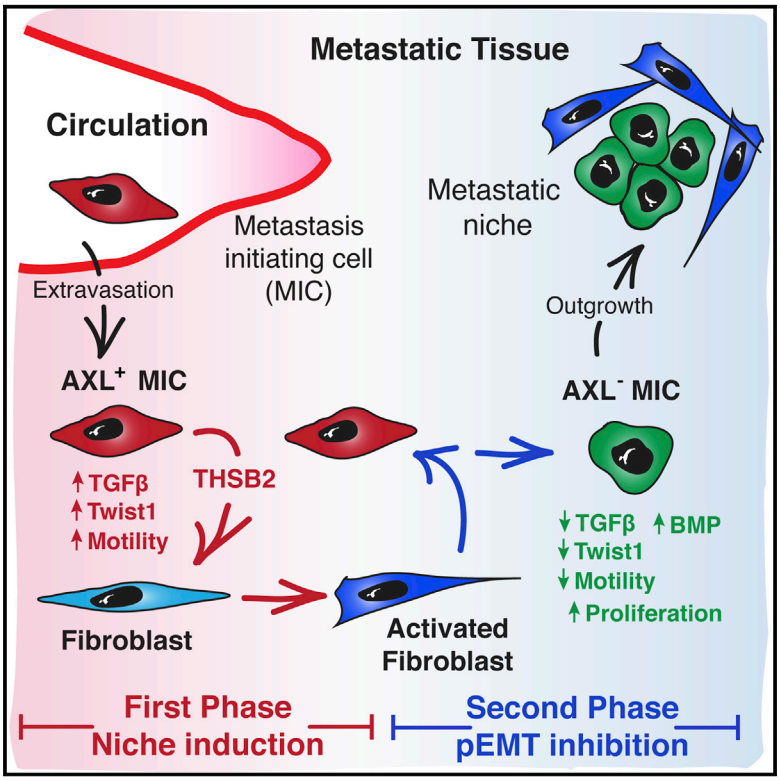

Authors

Yaiza del Pozo Martin, Danielle Park, Anassuya Ramachandran, ..., Caroline S. Hill, Erik Sahai, Ilaria Malanchi

Correspondence

ilaria.malanchi@crick.ac.uk

In Brief

del-Pozo-Martín et al. find that a mesenchymal state characterized by AXL expression triggers cancer cell-stromal cell crosstalk upon infiltration of the secondary site. These interactions affect metastatic colonization and, ultimately, lead cancer cell reversion to a more epithelial state.

Highlights

- AXL$^+$ mesenchymal-state cells have a higher capacity to activate fibroblasts
- AXL-EMT-dependent fibroblast activation is enhanced by THSB2
- Activated fibroblasts promote cancer cell plasticity toward a more epithelial state
- This epithelial shift is associated with a BMP-dependent growth

Accession Numbers

GSE63558

del Pozo Martin et al., 2015, Cell Reports *13*, 2456–2469
December 22, 2015 ©2015 The Authors
http://dx.doi.org/10.1016/j.celrep.2015.11.025

CrossMark

CellPress

OPEN ACCESS
CellPress

Cell Reports
Article

Mesenchymal Cancer Cell-Stroma Crosstalk Promotes Niche Activation, Epithelial Reversion, and Metastatic Colonization

Yaiza del Pozo Martin,[1] Danielle Park,[2] Anassuya Ramachandran,[3] Luigi Ombrato,[1] Fernando Calvo,[6] Probir Chakravarty,[4] Bradley Spencer-Dene,[5] Stefanie Derzsi,[2] Caroline S. Hill,[3] Erik Sahai,[2] and Ilaria Malanchi[1,*]
[1]Tumor-Stroma Interactions in Cancer Development
[2]Cell Biology of the Tumor Microenvironment
[3]TGF-β Superfamily Signalling in Development and Cancer
[4]Bioinformatics and BioStatistics Team
[5]Experimental Histopathology Unit
The Crick Institute, Lincoln's Inn Fields Laboratory, 44 Lincoln's Inn Fields, WC2A 3LY London, UK
[6]Tumor Microenvironment Team, Division of Cancer Biology, The Institute of Cancer Research, 237 Fulham Road, SW3 6JB London, UK
*Correspondence: ilaria.malanchi@crick.ac.uk
http://dx.doi.org/10.1016/j.celrep.2015.11.025
This is an open access article under the CC BY-NC-ND license (http://creativecommons.org/licenses/by-nc-nd/4.0/).

SUMMARY

During metastatic colonization, tumor cells must establish a favorable microenvironment or niche that will sustain their growth. However, both the temporal and molecular details of this process remain poorly understood. Here, we found that metastatic initiating cells (MICs) exhibit a high capacity for lung fibroblast activation as a result of Thrombospondin 2 (THBS2) expression. Importantly, inhibiting the mesenchymal phenotype of MICs by blocking the epithelial-to-mesenchymal transition (EMT)-associated kinase AXL reduces THBS2 secretion, niche-activating ability, and, consequently, metastatic competence. Subsequently, disseminated metastatic cells revert to an AXL-negative, more epithelial phenotype to proliferate and decrease the phosphorylation levels of TGF-β-dependent SMAD2-3 in favor of BMP/SMAD1-5 signaling. Remarkably, newly activated fibroblasts promote this transition. In summary, our data reveal a crosstalk between cancer cells and their microenvironment whereby the EMT status initially triggers and then is regulated by niche activation during metastatic colonization.

INTRODUCTION

Solid epithelial tumors are complex structures in which associated stromal cells, including fibroblasts, support cancer cells. During metastatic progression, cancer cells disseminate from their tissue of origin to re-establish the tumor structure in distant organs. Efficient metastasis requires the expression of specific molecules, such as POSTN and TNC, within the local microenvironment (Malanchi et al., 2012; Oskarsson et al., 2011). Therefore, a favorable microenvironment, or niche, is a crucial early requirement for metastatic progression (Sleeman, 2012). However, the factors that promote efficient metastatic niche activation remain poorly characterized.

Cancer cells display heterogeneity in intrinsic tumorigenic potential; only a small subset of cells within tumors retains the ability of sustaining long-term growth (Hermann et al., 2007; Malanchi et al., 2008) as well as triggering relapses (Chen et al., 2012). Cancer cells with the stem cell-like property of self-renewal can be defined functionally as cancer-initiating cells (CICs) for their capacity to elicit tumor growth. Moreover, metastatic initiating cells (MICs) can be distinguished from the bulk of cancer cells for their ability to establish metastasis. The functional assay for MICs involves determining the extent to which single cells can grow in a foreign tissue and is more challenging than the equivalent orthotopic transplantation assay used to assess the ability of CICs to initiate tumor growth. Although self-renewal ability is a common requirement for the re-initiation of a cancer cell mass at either primary or secondary sites, additional characteristics that discriminate MICs from CICs have not been explored. MICs have been identified previously in the mouse breast cancer model where mouse mammary tumor virus promoter controls the expression of the polyomavirus middle T antigen (MMTV-PyMT) (Malanchi et al., 2012). We hypothesized that, in addition to intrinsic tumorigenic potential, MICs would exhibit a higher capacity for interacting with their niche by activating naive cells at distant sites (Malanchi, 2013).

One strategy adopted by carcinoma cells to disseminate from the primary tumor mass is the activation of the developmental program epithelial-to-mesenchymal transition (EMT). During EMT, epithelial cells undergo a global change in cell architecture, leading to the loss of cell-cell adhesions in favor of cell-extracellular matrix (ECM) interactions and cell migration (Thiery et al., 2009). Notably, EMT modulations are not binary, but a graded range of intermediate states exists. The process is initiated by the activation of the EMT core transcription factors (TFs) Snail, Zeb, and Twist1 (Peinado et al., 2007), which drive epithelial cancer cells to switch off the expression of epithelial markers such as the adherens junction protein E-Cadherin and activate the expression of mesenchymal markers such as Vimentin. The tyrosine kinase AXL is a downstream effector of the EMT program (Vuoriluoto et al.,

2011). EMT in breast cancer cells triggers an increase in AXL expression, and inhibition of AXL reduces the invasive and tumorigenic behavior of cancer cells (Gjerdrum et al., 2010; Holland et al., 2010; Sheridan, 2013; Paccez et al., 2014).

Interestingly, the induction of EMT TFs correlates with the emergence of stem cell-like properties (Mani et al., 2008; Morel et al., 2008). This suggests that the gain of mesenchymal characteristics might not only affect dissemination from primary tumors but also boost the stem cell properties required for metastatic outgrowth. However, epithelial characteristics are re-acquired at metastatic locations via mesenchymal-to-epithelial transitions (METs), typically leading to the establishment of secondary tumors with epithelial phenotypes (Tsai et al., 2012). The outgrowth of metastases requires cancer cell self-renewal and growth ability. Therefore, in the context of metastatic growth, "stemness" is not strictly coupled to the mesenchymal features of cancer cells. The potential advantage of a more mesenchymal state of cancer cells at the metastatic site and the origin of their epithelial plasticity remain unclear.

In this study, we use breast cancer models to demonstrate that the EMT program is a key regulator of the enhanced niche activation capacity of MICs at secondary sites. We identify Thrombospondin 2 (THBS2) as a mesenchymal state-dependent effector of cancer cells that promotes stromal niche activation. Subsequently, the newly activated stroma promotes cancer cells to shift toward a more epithelial, BMP-dependent state compatible with proliferation. We elucidated a biphasic temporal regulation during metastatic colonization whereby the mesenchymal status of cancer cells promotes stromal activation, which, in turn, promotes cancer cell epithelial plasticity and their reversion to a more epithelium-like phenotype.

RESULTS

MICs Display Partial EMT Features

In the mouse breast cancer MMTV-PyMT model, MICs were identified by co-expression of the CD24 and CD90 markers (Malanchi et al., 2012). The gene expression profile of MICs ($CD24^+CD90^+$) was compared to that of non-MICs ($CD24^+CD90^-$) to generate a MIC signature (Figure S1A). We verified that high levels of Wnt signaling are a hallmark of metastatic cancer stem cells (Malanchi et al., 2008, 2012; Nguyen et al., 2009; Reya and Clevers, 2005; Vermeulen et al., 2010), along with other characteristics associated with their high metastatic potential, such as active transforming growth factor β (TGF-β) signaling (Padua et al., 2008) and Yap/Taz activity (Diepenbruck et al., 2014). We also found that the MIC signature exhibited characteristic features of EMT and its related extracellular matrix remodeling (Figure 1A and S1B). In line with this, MICs freshly isolated from primary tumors displayed a mesenchymal phenotype with higher expression of Vimentin and the EMT-related receptor AXL as well as reduced E-cadherin levels (Figures 1B and 1C). This more mesenchymal phenotype was corroborated functionally using Matrigel collagen matrices where MICs, either in pure or mixed non-MIC/MIC spheroids, displayed enhanced single-cell invasive behavior compared with non-MICs (Figures 1D, 1E, and S1C).

The capacity of MICs for invasion correlated with increased expression levels of actin cytoskeleton regulators and extracellular matrix components (Figures S1D and S1E). EMT in MICs was further confirmed by the higher expression and nuclear localization of EMT TFs (Figures S1F and S1G). However, the high level of heterogeneity within the MIC population suggests a graded EMT with intermediate "partial EMT" states rather than a simple binary transition. The MIC expression signature also correlated with different secretome gene sets (Figure 1A). Some of these secreted factors have been reported previously to play a role in metastasis, such as TNC, SPARC, or CCL2 (Oskarsson et al., 2011, Tichet et al., 2015; Qian et al., 2011).

We went on to investigate the influence that the observed partial EMT status of MICs has on their capacity for metastatic initiation following dissemination. Because the metastatic behavior of MMTV-PyMT MICs might be regulated by the activity of other pathways, such as WNT (Figure 1A), we selected a broader mesenchymal cancer cell pool expressing AXL, including the MIC ($CD24^+CD90^+$) population (Figure S2A). As expected, the $CD24^+AXL^+$ population isolated from primary tumors displayed partial mesenchymal features (Figures S2B and S2C). We next tested $CD24^+AXL^+$ cells for their cancer initiation and metastatic initiation potential using orthotopic transplantation and tail vein injection, respectively (Figures 1F and 1G). Both assays require cancer cell stemness to reinitiate and sustain a cancer cell mass, either in a collective challenge within their organ of origin with favorable niches or when seeded via circulation as single cells in a likely less favorable "foreign" organ. We observed no difference in primary tumor growth for $CD24^+AXL^+$ and $CD24^+AXL^-$ cells, indicating that the subpools exhibit a comparable capacity for cancer initiation (Figure 1H). Indeed, for MMTV-PyMT tumor cells, more mesenchymal characteristics do not appear to influence tumor initiation ability. The more epithelial $CD24^+SCA1^+$ subpool (Figures S2D–S2F) identified previously for their tumor initiation capacity (Liu et al., 2007) displayed a similar tumor initiation potential as the more mesenchymal $CD24^+AXL^+$ or MIC pools (Figures S2G–S2I). Strikingly, $CD24^+AXL^+$ cancer cells show a higher lung metastasis competence compared with their more epithelial counterparts (Figure 1I). This suggests that the common mesenchymal characteristics observed within the $CD24^+AXL^+$ and MIC $CD24^+CD90^+$ cancer cells might be linked functionally to their metastatic competence, independent of an advantage in intrinsic stemness potential displayed in a favorable microenvironment.

MICs Promote Quicker Lung Fibroblast Activation

The highly secretory mesenchymal status of MICs might provide an increased capacity of generating a favorable environment, or niche, in distant sites (Figure 1A). We examined this suggestion by analyzing the activation of lung stromata around disseminated AXL^+ or AXL^- cancer cell early after their extravasation into the lungs. In line with our hypothesis, $CD24^+AXL^+$ cells are surrounded by higher numbers of smooth muscle actin (SMA)-activated fibroblastic stroma compared with $CD24^+AXL^-$ cells. We observed no difference in their tissue localization, in particular in their proximity to lung endothelial cells (Figures 2A–2D). To test whether niche activation ability is a common advantage conferred by the mesenchymal status of $CD24^+AXL^+$ and MIC pools, we measured the ability of isolated MICs to trigger features of cancer-associated fibroblasts (CAFs) in normal lung fibroblasts ex vivo. Sorted MICs or

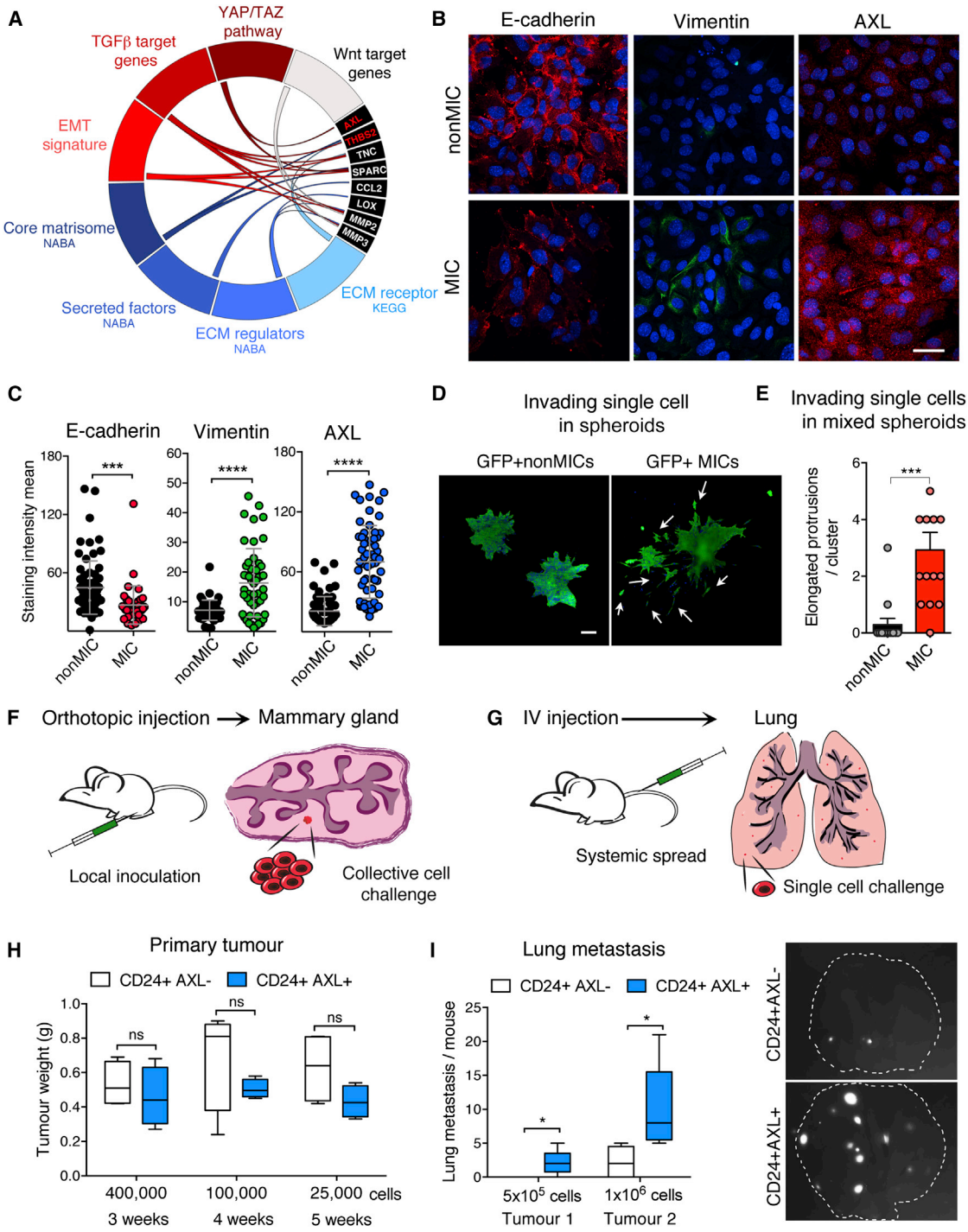

Figure 1. The Mesenchymal Features of MICs Are Part of Their Metastasis-Initiating Potential

(A) Circos plot displaying selected gene signatures correlating positively with MIC-upregulated genes (see also Figures S1A and S1B). Black blocks highlight metastasis-promoting genes either known (white) or described in this study (red).

(B and C) Representative immunofluorescence images (B) of non-MICs ($CD24^{+}CD90^{-}$) and MICs ($CD24^{+}CD90^{+}$) stained with E-cadherin, Vimentin, and AXL antibodies. Scale bar, 40 μm. Staining quantification is shown in (C). Data are from one representative experiment of five.

(D) Spheroid invasion assay. Shown are representative fluorescence images of MIC or non-MIC spheroids from actin-GFP/PyMT tumors in Matrigel:collagen I. Scale bar, 100 μm.

(E) Mixed spheroid invasion assay. The histogram shows the number of cells invading as single cell (1:9 actin/GFP MICs:non-labeled non-MICs) in Matrigel:collagen I (see also Figure S1C).

(legend continued on next page)

non-MICs with a GFP-labeled normal lung fibroblast cell line (NLF3) were plated and monitored for the induction of early fibroblast activation markers (Figure 2E). Because all cancer cells are capable of fibroblast activation to some extent, we used low cell numbers to increase the assay's sensitivity. After 24 hr, fibroblasts co-cultured with MICs exhibited early nuclear YAP translocation, required for CAF induction, and higher fibroblast activation protein (FAP) expression compared with fibroblasts cultured with non-MICs (Figures 2F–2H; Calvo et al., 2013). To verify that the induction of these markers represents fibroblast activation, we performed functional gel contraction assays to examine the ability of fibroblasts to physically remodel the ECM. Limited numbers of cell-sorted MICs or non-MICs from primary tumors were seeded in the upper chamber of a trans-well dish. In the lower chamber of the co-culture, normal lung fibroblasts (NFs) freshly isolated from wild-type mouse lungs were embedded in collagen-Matrigel matrices (Figure 2I). Importantly, we observed that MICs trigger significantly greater fibroblast-driven gel contraction compared with the other primary cancer cells (Figures 2J). In parallel, a gain of a CAF gene expression signature was induced in fibroblast co-cultured with MICs. Collectively, these data provide direct evidence that cancer cells displaying partial EMT characteristics show an enhanced ability to generate activated fibroblasts, a crucial component of the metastatic niche.

Thrombospondin 2 Secretion Increases Stromal Activation Capacity and Confers a Metastatic Advantage in MICs

To understand the mechanism underlying the enhanced capacity for fibroblast activation, we tested several MIC-specific secreted proteins for their ability to activate fibroblasts (Figures S3A and S3B). We found that purified recombinant THBS2 significantly enhanced the gel contraction capacity of fibroblasts (Figure 3A). We observed that exposure of lung fibroblasts to purified THBS2 led to activation of integrin β1 and the phosphorylation of its downstream effector focal adhesion kinase (pFAK) (Figures 3B and 3C). Importantly, a specific integrin β1-blocking antibody (β1BA) arrested the THBS2-dependent integrin cascade as well as fibroblast activation (Figures 3B–3D). To examine the role THBS2 might play in tumorigenicity, we used a specific short hairpin RNA (shRNA) targeting *Thbs2* mRNA (shTHBS2) to knock down its expression in primary MMTV-PyMT cancer cells (PyMT) (Figure 3E). Importantly, THBS2 depletion rendered cancer cells less able to activate lung fibroblasts (Figure 3F). Furthermore, shTHBS2 cancer cells were reduced dramatically in their capacity for lung metastatic colonization upon intravenous injection (Figure 3H). However, this is unlikely to be due to an effect on intrinsic cancer cell stemness because shTHSB2 PyMT cells maintained their ability to initiate early primary tumor growth in vivo or form spheres in vitro (Figure 3G and S3C). Similar findings were obtained using a second shRNA to block THBS2 secretion (Figures S3D–S3H). Because THBS2 is highly expressed in only a subset of PyMT cells, we tested the consequence of exogenous *Thbs2* gene expression in all PyMT cells. Importantly, broad THBS2 secretion resulted in increased early metastatic growth in the lungs upon direct seeding (Figure 3I). These data support the clinical correlation of high *Thbs2* expression with poor prognosis in advanced-stage human breast cancers (Figure S3I). Together, these results suggest that MICs mediate efficient fibroblast activation through THBS2 secretion and that this is critical for efficient metastatic initiation within the secondary tissue.

The Niche Activation Capacity of Metastatic Cancer Cells Depends on Their Partial Mesenchymal Status

The previous results reveal high niche activation ability as a crucial characteristic of MICs. Interestingly, we also found that their partial EMT phenotype defined by AXL expression was sufficient to determine their metastatic competence (Figure 1I). Therefore, we investigated whether the high niche activation ability of MICs is linked functionally to their AXL mesenchymal status. We used two approaches to downregulate AXL. First we used the AXL-specific small molecule inhibitor R428 (Holland et al., 2010), and second we used an shRNA to target *Axl* mRNA (Gjerdrum et al., 2010). Brief exposure of MICs to R428 triggered an overall shift toward a more epithelial phenotype with lower Vimentin and AXL expression and higher E-cadherin levels (Figures 4A, 4B, and S4A). Accordingly, we detected a reduction in the expression of EMT-TFs and motility in MICs (Figures S4B and S4C). Similar phenotypic changes occurred in the basal human breast cancer cell line MDA-MB-231 (MDA231) following treatment with R428. Indeed, although MDA231 cells, which homogeneously express AXL, typically display mesenchyme-like features, a single pulse of R428 reduced the expression of AXL and Vimentin and cell motility for up to 48 hr (Figures S4D–S4G). Interestingly, upon R428-mediated mesenchymal inhibition, cancer cells also reduced the expression of secreted factors, including THBS2 (Figures 4C and S4H). Concomitantly, the fibroblast activation ability of R428-treated metastatic cells was impaired dramatically (Figure 4D). Because similar results were found using an shRNA against *Axl* mRNA in primary PyMT cells (Figure S5A), we can exclude non-specific effects of the small molecule inhibitor R428. Indeed, shRNA-induced AXL downregulation in PyMT cells reduced THBS2 secretion and ex vivo fibroblast activation abilities (Figures 4E and 4F). Notably, the expression of *Thbs2* appears to be highly linked to the expression of the *Axl* and *Twist1* genes in human tumor biopsies (Figure S4I). These data demonstrate that the mesenchymal status of MICs is directly related to their enhanced capacity for fibroblast activation.

(F and G) Schematic showing a collective cell challenge for primary tumor growth into mammary fat pads (F) or a single-cell challenge for lung metastasis via the tail vein (G).

(H) Box plot showing the primary tumor burden in grams generated by the indicated sorted cells after overnight culture. Shown are data from three experiments using the indicated cell numbers (n = 4/group). IV, intravenous.

(I) Box plot showing the lung metastatic burden 5 weeks after tail vein injection. Two independent experiments are shown (n = 5–6/group). Shown are representative images of lungs with GFP^+ metastases.

Error bars represent SD in (C) and SEM in all other plots. *p < 0.05; ***p < 0.001; ****p < 0.0001; ns, not significant.

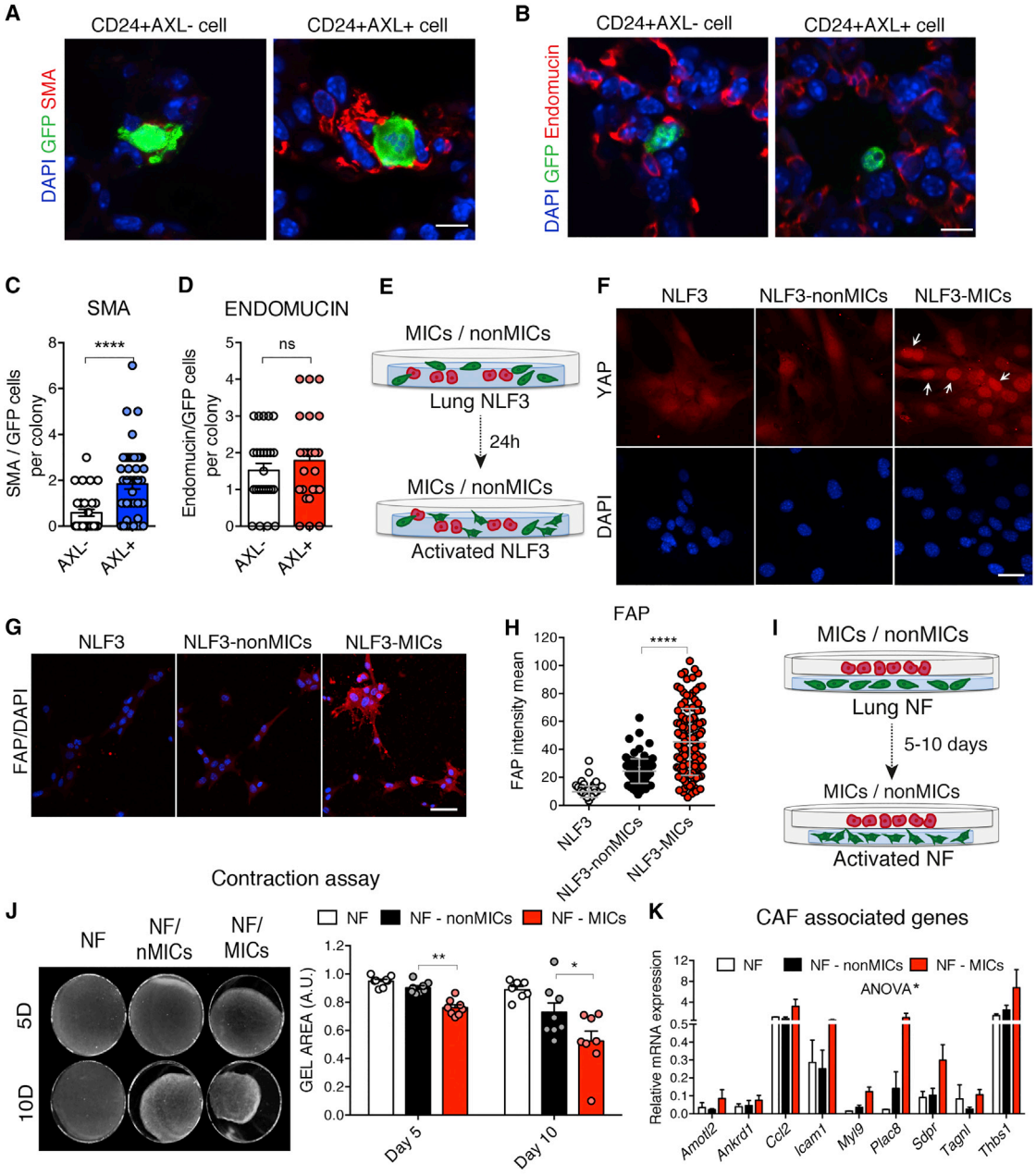

Figure 2. MICs Have a Higher Capacity to Activate Fibroblasts

(A–D) Representative pictures showing single GFP$^+$ cells (green) from the indicated subpools 72 hr after intravenous injection into RAG1-deficient mice. (A) DAPI staining (blue) and SMA (red); quantified in (C). (B) DAPI staining (blue) and Endomucin (red); quantified in (D). Scale bars, 10 μm. n = 32–50 cells.

(E) Schematic of the cancer cell and GFP$^+$ normal lung fibroblast cell line (NLF3) co-culture setting.

(F and G) Representative images of (F) early YAP nuclear translocation in NLF3 or (G) FAP levels in NLF3 cells 24 hr after plating. Scale bars, 40 μm (F), 70 μm (G).

(H) Chart indicating the levels of FAP in NLF3 cells from (G). Data are from one representative experiment of three.

(I) Schematic displaying the cancer cell and NLF3 co-culture setting.

(J) Representative images of the gel contraction by NLF3 assayed as in (I). The histogram shows the gel area of three independent experiments (n = 8/group).

(K) Quantitative real-time PCR analysis of the levels of CAF-defining genes in primary NF after co-culture with MICs (NF-MIC) or nonMICs (NF-nonMIC). Data are from at least three experiments in triplicate normalized to *Gapdh*. p = 0.0235 by ANOVA comparing differences between the NF, NF-non-MIC, and NF-MIC gene signatures.

Error bars represent SD in (H) and SEM in all other plots. *p < 0.05, **p < 0.01, ****p < 0.0001. ns, non-significant.

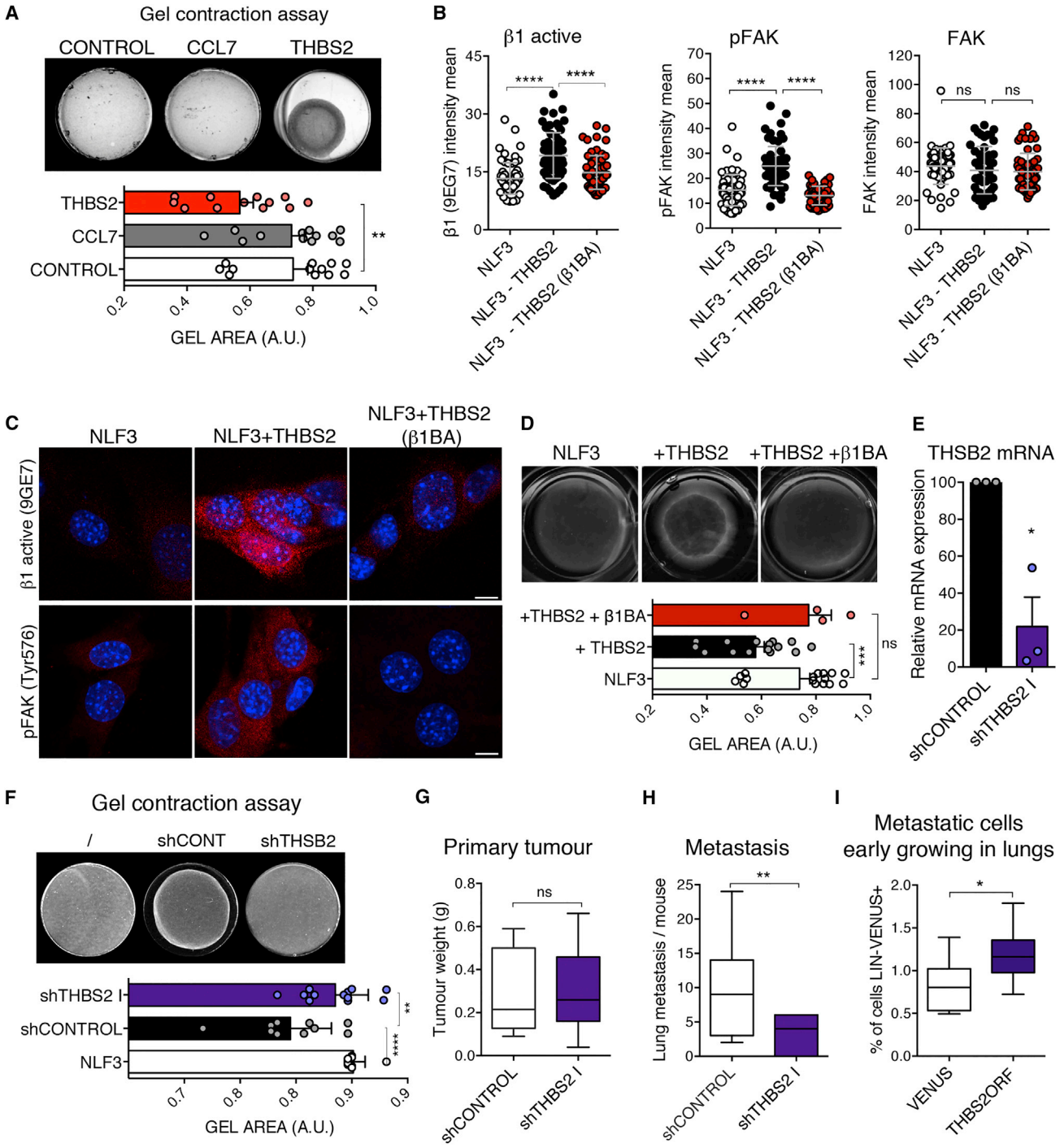

Figure 3. Cancer Cell-Derived THBS2 Enhances Fibroblast Activation

(A) Gel contraction induced by NLF3 after 3 days of exposure to recombinant CCL7 or THBS2. Top: representative NLF3-gels. Bottom: gel area quantification of three independent experiments (n = 12/group).

(B and C) Levels of the active isoform of integrin β1 (clone 9EG7) and its downstream effector FAK (total or phosphorylated) in NLF3 for the indicated groups. Data are from one representative experiment of two. Quantification is shown in (B) and representative images in (C). Scale bars, 20 μm.

(D) Gel contraction induced by NLF3 after co-culture with recombinant THBS2 with or without integrin β1-blocking antibody. Top: representative NLF3-gels. Bottom: gel area quantification of two independent experiments (n = 4–16/group).

(E) Quantitative real-time PCR analysis of the mRNA expression level of *Thbs2* by the indicated cells. Data are from three different experiments in triplicate normalized to Gapdh.

(legend continued on next page)

Cancer Cells Require AXL Mesenchymal Features to Facilitate Fibroblast Activation

We showed that MICs isolated from primary tumors are in an AXL-positive mesenchymal state. Therefore, we went on to examine the mesenchymal status of cancer cells at the target site by monitoring AXL expression during early colonization. We detected two distinct phases of AXL expression: a first phase, where the PyMT EMT MIC subpool maintains AXL, and a second phase, where the AXL-positive phenotype is lost coincidentally with MIC expansion in the lungs (Figure 5A). Similar biphasic AXL expression was observed in the MDA231 cell line (Figure 5B). Because the ability of cancer cells to trigger the niche is crucial for metastatic establishment (Figure 3) and dependent on the mesenchymal phenotype (Figure 4), we assessed whether the maintenance of AXL is required for the first phase of metastatic colonization. To do this, we inhibited AXL activity only during the first colonization phase by pre-treating cancer cells with the R428 inhibitor prior to intravenous injection and continued treatment in vivo for 7 days (Figure 5C and S5B). Notably, although R428 pre-treatment did not alter cancer cell extravasation (Figure S5C), it did significantly reduce metastasis after 5 weeks (Figures 5D–5F). Remarkably, only R428 pre-treatment 24 hr before seeding into the lung was sufficient to inhibit metastatic establishment (Figure 5E), suggesting that AXL mesenchymal features are required early after metastatic cell arrival to new tissue. Although short-term inhibition of AXL decreased metastatic competence, this had no effect on proliferation, self-renewal, and 3D cancer cell mass growth in vitro (Figures S5D–5G), or primary tumor initiation in vivo (Figure S5H). Interestingly, enhancing THBS2 expression in the MDA-MB-231 cell line partially rescued metastasis upon AXL inhibition in spite of the fact that THBS2 overexpression only provided a positive trend toward metastasis in these cells (Figures 5G, S5I, and S5J). This result is in line with the observation that AXL-mesenchymal cells show a THBS2-mediated advantage in niche activation. We also observed a block in metastasis upon AXL inhibition using shRNA knockdown in PyMT cells (Figures 5H and 5I). Furthermore, treatment of a second mouse breast cancer cell line (4T1) with shTHBS2 or shAXL also reduced the metastatic ability of 4T1 cells (Figures S5K and S5L). Together, these results suggest that the first phase of metastatic colonization requires the niche activation capacity provided by the AXL mesenchymal characteristics.

Activated Stroma Modulates the EMT of Cancer Cells toward a More Epithelial State

The previous results highlight the requirement of a mesenchymal state for metastatic initiation upon seeding at the target site. However, when cancer cells start growing within the metastatic tissue, AXL expression is downregulated (Figures 5A, 5B, and 6A). ImageStream analysis showed that, coincident with AXL downregulation, GFP^+ cancer cells growing in the lungs exhibit reduced expression of the EMT transcription factor Twist1 (Figures 6B, 6C, S6A, and S6B). This suggests that the previously reported EMT inhibition at the secondary site (Tsai et al., 2012) is controlled temporally within the second phase of metastatic colonization. Therefore, we investigated the changes that occur in metastatic cells during this time period.

Ex vivo co-culture (as shown in Figure 2E) demonstrated that, concomitant with fibroblast activation (Figures 2F–2H), MICs express lower levels of *Axl*, *Twist1* (Figures 6D and 6E), and overall EMT TF mRNA (Figure S6C). To track the phenotypic changes during this time, cancer cells were co-cultured with CAFs for 24 hr under adherence conditions (Figure S6D). Here we found that MICs reduced expression of Vimentin and AXL and increased expression of E-cadherin (Figures S6E and S6F). These results suggest that crosstalk between fibroblasts and cancer cells triggers alterations in both compartments; namely, activation of fibroblasts and consequent reacquisition of epithelial characteristics by cancer cells. To functionally validate these changes in the MIC EMT state, we analyzed their 3D invasion modality as they first come in contact with CAFs. In line with previous studies (Gaggioli et al., 2007; Yu et al., 2014), carcinoma cells in a non-invasive epithelial state (non-MICs) activated both single and collective cell invasion modalities. Strikingly, in line with the downregulation of mesenchymal markers, MICs displayed a notable reduction in single-cell migration when surrounded by CAFs (Figures 6F and 6G).

We next investigated the potential molecular mechanism of CAF-driven changes in cancer cells. TGF-β signaling has been implicated extensively in metastasis (Padua et al., 2008). High TGF-β signaling favors early metastatic colonization, whereas its subsequent reduction is important for metastatic outgrowth (Giampieri et al., 2009). Because TGF-β signaling, which is active in MICs (Figure 1A and S1B), could be linked functionally to their mesenchymal status (Diepenbruck et al., 2014), we assessed whether modulation of TGF-β signaling in MICs associates with the reacquisition of more epithelial characteristics. Using ImageStream analysis, we monitored the dynamics of activation of the TGF-β effector SMAD2-3 in metastasizing cells in vivo. As AXL^+ mesenchymal cells in the lung transit from the first to the second phase of colonization, the number and staining intensity of $pSMAD2\text{-}3^+$ cells decreased similarly to Twist1 expression (Figure 6H, S6G, and S6I). These data are in agreement with the previous evidence showing that a reduction in TGF-β signaling is required for the acquisition of the proliferative status necessary for metastatic outgrowth (Massagué, 2008). Conversely, the activation levels of BMP-dependent pSMAD1-5 was maintained during the second phase of colonization, and the number of $pSMAD1\text{-}5^+$ cells increased (Figures 6I, S6H, and S6J). In line

(F) Gel contraction induced by NLF3 after co-culture with the indicated cancer cells. Top: representative NLF3-gels. Bottom: gel area quantification of two independent experiments (n = 10–12/group).
(G) Box plot showing early primary tumor growth of primary PyMT cells expressing shCONTROL or shTHBS2 constructs in an orthotopic challenge (n = 6/group).
(H) Box plot showing the metastatic burden from PyMT cells expressing shCONTROL or shTHBS2 constructs 5 weeks after tail vein injection (n = 7–11/group). The superficial lung metastasis number was evaluated.
(I) Box plot displaying the metastatic cell content by flow cytometry 20 days after tail vein injection of PyMT control or THBS2ORF-expressing cells (n = 8/group).
Error bars represent SD in (B) and SEM in all other plots. *$p < 0.05$, **$p < 0.01$, ***$p < 0.001$, ****$p < 0.0001$.

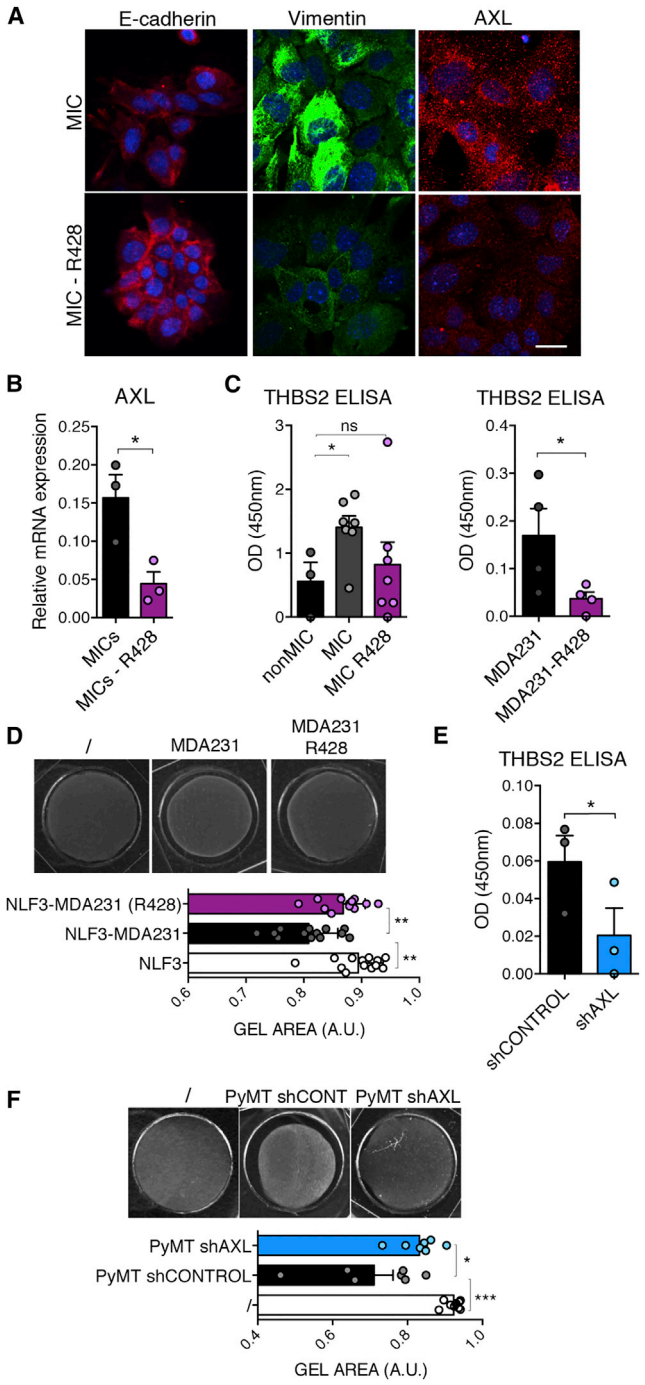

Figure 4. The Mesenchymal Status of Cancer Cells Drives Fibroblast Activation

(A) Representative images showing the expression of E-cadherin, Vimentin, and AXL in MICs 24 hr after treatment with DMSO or R428. Scale bar, 20 μm. See also Figure S4A.

(B) *Axl* gene expression levels in PyMT cells pre-treated with or without R428 as determined by quantitative real-time PCR analysis. Data are from three different experiments in triplicate (normalized to *Gapdh*).

(C) THBS2 secretion in the media collected from the indicated cancer cells 24 hr after R428 pre-treatment as measured by ELISA. Left: PyMT subpools, non-MIC data from three experiments in duplicate; MIC ± R428 treatment, data from seven experiments in duplicate. Right: MDA-MB-231 cell line (MDA231), data from four experiments in duplicate.

(D) Gel contraction induced by NLF3 after exposure to MDA231 pre-treated with DMSO or R428. Top: representative NLF3 gels. Bottom: gel area quantification of three independent experiments (n = 12/group).

(E) THBS2 secretion in the media collected from the indicated cancer cells 24 hr after plating by ELISA. Data are from three different experiments in duplicate.

(F) Gel contraction induced by NLF3 after exposure to the indicated cells. Top: representative NLF3 gels. Bottom: gel area quantification of two independent experiments (n = 7–9/group).

Error bars represent SEM. *$p < 0.05$, **$p < 0.01$, ***$p < 0.001$. ns, non-significant.

with this, we observed that the levels of inhibitor of differentiation 1 (ID1), a BMP/pSMAD1-5 target gene needed for cell proliferation during metastatic outgrowth (Gupta et al., 2007), were maintained, in particular in Twist1^{-} cells (Figures 6J and 6K). Notably, this modulation of ID1 in cancer cells could be recapitulated in vitro by exposure to CAF-conditioned medium (CaCM), which increases the levels of ID1 in a BMP-dependent manner (Figures 6L and 6M). Importantly, treatment with the specific inhibitor LDN193189 in vivo resulted in reduced metastatic capacity (Figures 6N and 6O), suggesting that BMP/pSMAD1-5 activity does indeed play a significant role in the second phase of colonization.

Together, these data show that, in the second colonization phase, the phenotypic changes observed in metastasizing cancer cells toward a more epithelial state correlate with an inhibition of TGF-β signaling and the enhanced BMP signaling necessary for metastatic outgrowth.

The Second Metastatic Colonization Phase Requires Temporal Regulation for Efficient Metastatic Establishment

We showed that the mesenchymal status of cancer cells during the first phase of colonization is required for metastatic establishment. However, when CD24^{+}AXL^{+} mesenchymal cancer cells accumulate in the lung, they revert to an AXL-negative, more epithelial state (Figure 5) following interaction with newly activated fibroblasts (Figure 6). If these two events were linked causally, then it would be expected that a temporal regulation of epithelial plasticity is critical for metastatic outgrowth. Initially, to probe this hypothesis, we induced an early mesenchymal reversion of metastatic cells by R428 treatment during the second phase of colonization (Figure 7A). This AXL inhibition no longer blocks the metastatic establishment of MDA231 cells (Figure S7A) and increases metastasis of primary PyMT cells (Figures 7B and 7C), suggesting that inhibiting EMT in this phase promotes metastasis. We observed that AXL inhibition in late-stage metastases did not alter the number of metastatic nodules (Figures 7A and 7B). Next, we delayed mesenchymal reversion in vivo by exogenous expression of the *Axl* gene (LTR-AXL) in cancer cells (Figure 7D). This leads to an exacerbated AXL-positive mesenchymal phenotype (Figures 7G, 7J, and S7B) without altering the proliferation capacity (Figure S7C). Importantly, preventing early AXL downregulation in metastasizing LTR-AXL-expressing cells delayed initial growth in the lungs (Figures 7E and 7F) and, ultimately, led to a reduction in the metastatic potential of both PyMT and MDA231 cancer cells (Figures 7H, 7I, and 7K). These data support the idea that downregulation of AXL is

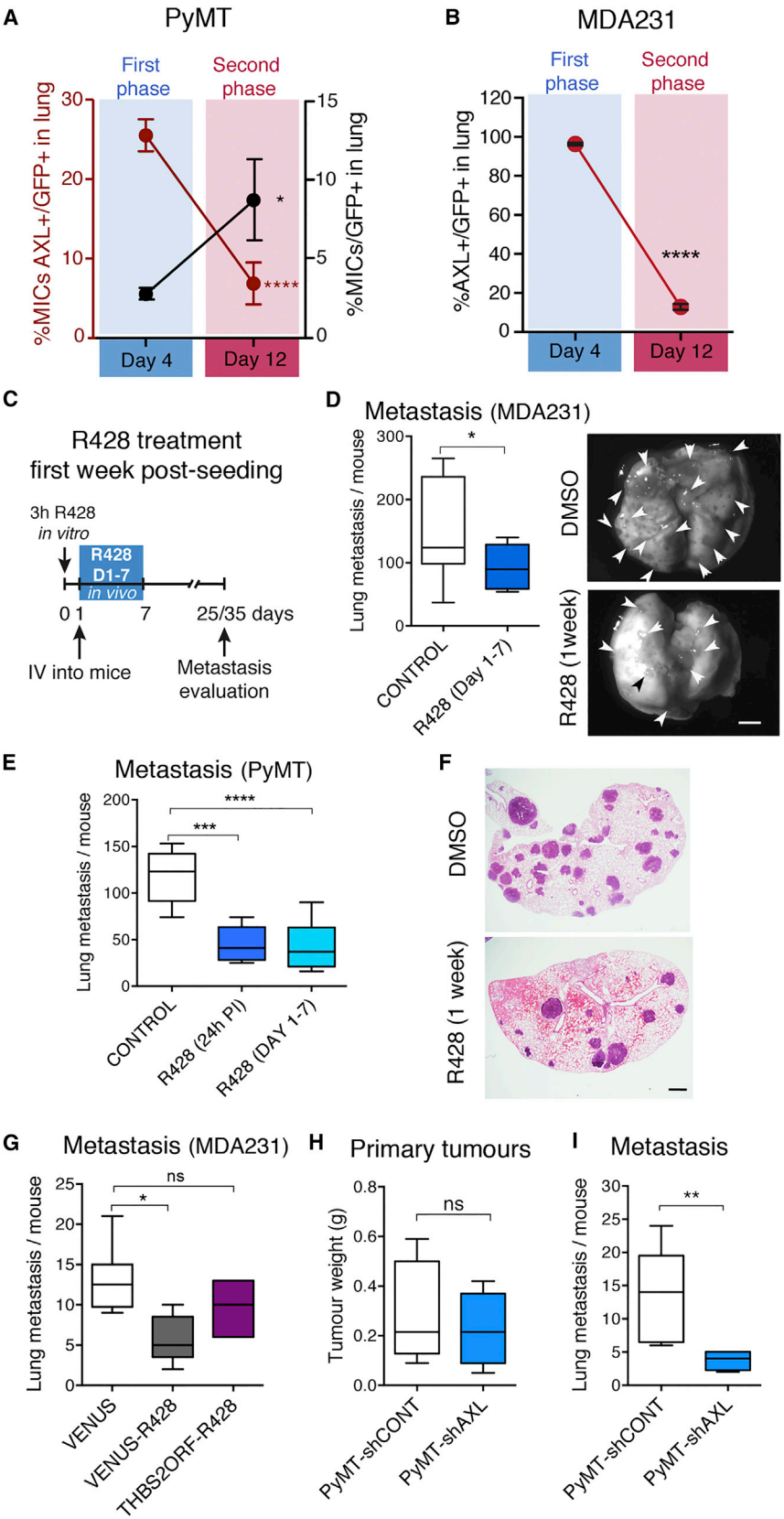

Figure 5. The Mesenchymal Status Is Regulated Temporally during Metastatic Colonization

(A) Flow cytometry analysis of the percentage of AXL$^+$ MICs (red, left y axis) and total MICs (black, right y axis) among total GFP$^+$ cancer cells in the lung 4 and 12 days after tail vein injection (n = 8–9/group from two independent experiments).

(B) Flow cytometry analysis of the percentage of AXL$^+$GFP$^+$ MDA-MB-231 cells (MDA231) among total GFP$^+$ cancer cells in the lung 4 and 12 days after tail vein injection (n = 3/group).

(C) Schematic of the R428 treatment setting for PyMT or MDA231 cells. IV, intravenous.

(D) Box plot showing the metastatic burden of MDA231 cells exposed to DMSO (n = 13) or R428 (n = 8) during the first week of colonization. The superficial lung metastasis number was evaluated. Shown are representative pictures of metastatic lungs. Scale bar, 300 μm.

(E) Box plot displaying the metastatic burden of PyMT cells pre-treated with DMSO (n = 14) or R428 (n = 5). In the last group (light blue, n = 9) mice were additionally treated with R428 during the first week of colonization. The superficial lung metastasis number was evaluated.

(F) Representative H&E staining of metastatic lung sections from the indicated mice. Scale bar, 100 μm.

(G) Box plot showing the metastatic burden of control (Venus) or THBS2-expressing MDA231 cells treated as in (C) (n = 7–5/group). Micrometastases were evaluated in histological sections of one lung lobe (see also Figure S5J).

(H) Box plot displaying early primary tumor growth after orthotopic transplantation of the indicated primary PyMT cells (n = 6/group).

(I) Box plot showing the metastatic burden of the indicated PyMT cells after tail vein injection (n = 5–8/group). The superficial lung metastasis number was evaluated.

Error bars represent SEM. *p < 0.05, **p < 0.01, ****p < 0.0001. ns, non-significant.

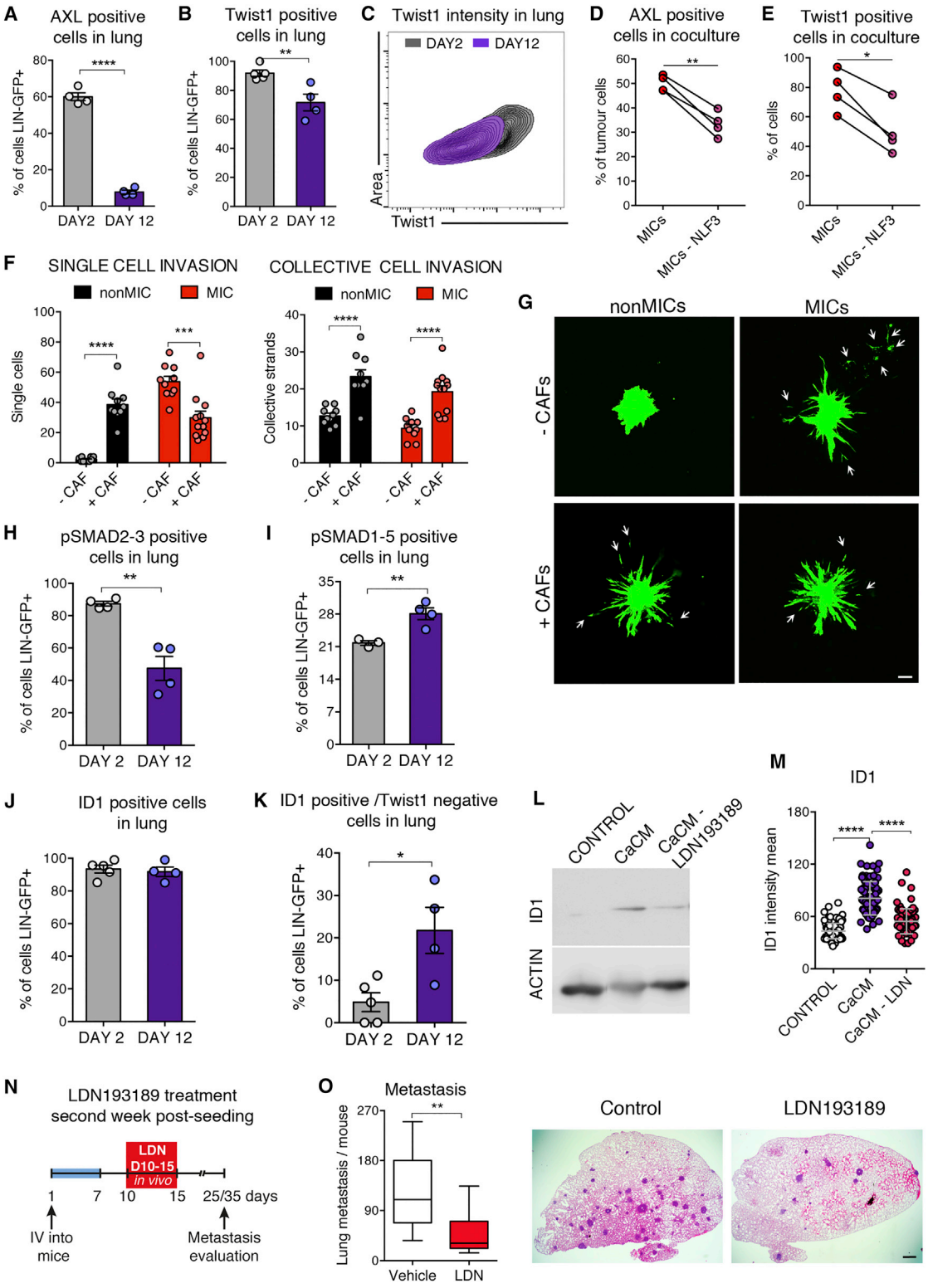

Figure 6. Attenuation of the Metastatic Cell Mesenchymal Phenotype

(A) Flow cytometry analysis changes in AXL$^+$ cancer cells seeded in the lungs after the indicated times points (n = 8–9/group). Data are from one representative experiment of two.

(legend continued on next page)

required during the second colonization phase to allow the transition to a more epithelial proliferative state. Interestingly, the overexpression of AXL in cancer cells led to a reduction in metastatic capacity specifically because an enhancement of primary tumor growth was detected (Figure S7D). This is likely due to an increase in AXL tyrosine kinase receptor activity at the early stages of tumor initiation, leading to the generation of larger tumors without obvious histologic changes after tumor establishment (Figures S7E and S7F).

DISCUSSION

Successful establishment of metastases requires cancer cells with self-renewal properties to disseminate from their tissue of origin and re-initiate growth at secondary sites. The evidence that experimental induction of EMT in epithelial cells triggers stem cell characteristics suggests a unified mechanism for cancer metastasis. However, the plasticity of the EMT program from dissemination to distant colonization during the metastatic process makes the direct relationship between EMT and stemness controversial (Tsai et al., 2012; Mani et al., 2008; Morel et al., 2008; Wellner et al., 2009; Brabletz, 2012; Nieto, 2013) and suggests that metastatic cancer cells are likely to undergo a partial EMT that can be modulated toward a more mesenchymal or epithelial state (Ombrato and Malanchi, 2014). Furthermore, although the requirement of an EMT inhibition at the metastatic site has been reported previously (Tsai et al., 2012), the dynamic regulation of the mesenchymal/epithelial transition is currently unknown. Using breast cancer models, we highlight the importance of the more mesenchymal phenotype of MICs during the early phase of metastatic colonization. Moreover, we demonstrate the requirement for AXL mesenchymal state-dependent THBS2 secretion in mediating enhanced niche activation. We also identify a subsequent phase of colonization where the mesenchymal phenotype of cancer cells is downmodulated by the interaction with the newly induced niche. This crosstalk leads to inhibition of TGF-β signaling and pSMAD1-5-dependent outgrowth, shifting cancer cells toward a more epithelial and proliferative state. Blocking the effectors of these pathways during this biphasic process reduces metastasis: THBS2 expression during the first phase or pSMAD1-5 activity during the second phase. Here we identify epithelial plasticity as a crucial determinant of metastatic colonization and describe how disruption of AXL-dependent phenotypic modulation is sufficient to reduce metastatic efficiency.

In agreement with the previously observed link between the EMT program and the gain in stemness (Mani et al., 2008; Morel et al., 2008), we found that the MICs of the MMTV-PyMT tumor model (Malanchi et al., 2012) display a mesenchymal phenotype (Figure 1A–1D and S1). However, using the EMT downstream effector AXL as a marker for mesenchymal cancer cells, we demonstrate that, within the MMTV-PyMT hierarchy, the mesenchymal features per se do not confer a differential tumor initiation ability (Figure 1H and S2). Nonetheless, a more mesenchymal state promotes growth at a less favorable distant environment (Figure 1I). This correlates with a higher capacity of $CD24^+AXL^+$ cells to induce stromal activation early after infiltration of the secondary tissue (Figures 2A–2D). Our work suggests that the increased intrinsic ability to trigger a favorable microenvironment at the naive target site provides a metastatic initiation advantage. Indeed, both the MIC subpool of MMTV-PyMT cancer cells as well as the metastatic human MDA-MB-231 cell line show higher niche component activation ability according to their mesenchymal phenotype (Figures 2 and 4) and THBS2 secretion (Figure 3). We show here that THBS2 is capable of triggering fibroblast activation via integrin signaling and enhancing early metastatic colonization (Figure 3I). This finding is supported by computational analyses defining *Thbs2* as one of the three genes associated with a stromal desmoplastic reaction and high metastatic risk (Kim et al., 2010) as well as by the clinical evidence of its correlation with poor prognosis in high-grade human breast cancers (Figure S3I). However, in rare circulating cancer cell clusters that exhibit high metastatic potential, the mechanism we describe may be circumvented (Aceto et al., 2014). In this context, the cells within the cluster may create their own favorable niche and, therefore, bypass the requirement for a mesenchymal state and associated niche activation.

Our results support the concept that stemness is unperturbed by the mesenchymal/epithelial plasticity of metastatic cells and correlate with a flexible partial EMT state rather than with a stable binary EMT program. We confirmed that, to efficiently generate a cancer cell mass at a distant site, cells regain a more epithelial phenotype (Tsai et al., 2012). Notably, we now show that this modulation is controlled temporally during the second phase of metastatic

(B and C) ImageStream analysis changes in Twist1 expression in AXL^+ cancer cells seeded in the lungs after the indicated times points (n = 4–5/group). (B) Quantification of $Twist1^+$ cells from one representative experiment of three. (C) Contour plot of representative lungs from (B) showing Twist1 staining intensity. (D and E) MIC changes after 3–5 days of co-culture with NLF3 as in Figure 2E. (D) Flow cytometry quantification of AXL expression levels. Data are from one representative experiment (n = 4/group) of two. (E) ImageStream analysis of the percentage of $Twist1^+$ cells. Data are from one representative experiment (n = 4/group) of two.

(F and G) Spheroid invasion assay. Labeled MIC or non-MIC (green) spheroids were imaged 48 hr after seeding into Matrigel:collagen I with or without CAFs. (F) Quantification of single (left) and collective (right) cell invasion. Data are from one representative experiment of two. (G) Representative spheroid images. Arrows indicate single invading cells. Scale bar, 100 μm.

(H–K) ImageStream analysis of $pSMAD2\text{-}3^+$ (H), $pSMAD1\text{-}5^+$ (I), $ID1^+$ (J), and $ID1^+Twist1^-$ (K) cell percentages in the lung 2 or 12 days post-seeding (n = 3–5/group).

(L and M) Expression levels of ID1 in primary $CD24^+AXL^+$ tumor cells 24 hr after exposure to the indicated media and in the presence of LDN193189 inhibitor determined by (L) western blot using Actin as a loading control (one representative experiment of two) or (M) immunofluorescence staining quantification (one representative experiment of two).

(N) Schematic showing the in vivo LDN193189 treatment setting.

(O) Box plot displaying the metastatic burden of PyMT cells in mice treated with vehicle or LDN193189. Shown are representative H&E-stained lung sections (n = 9–12/group). Scale bar, 100 μm.

Error bars represent SD in (M) and SEM in all other plots. *p < 0.05, **p < 0.01, ***p<0.001, ****p < 0.0001. ns, non-significant.

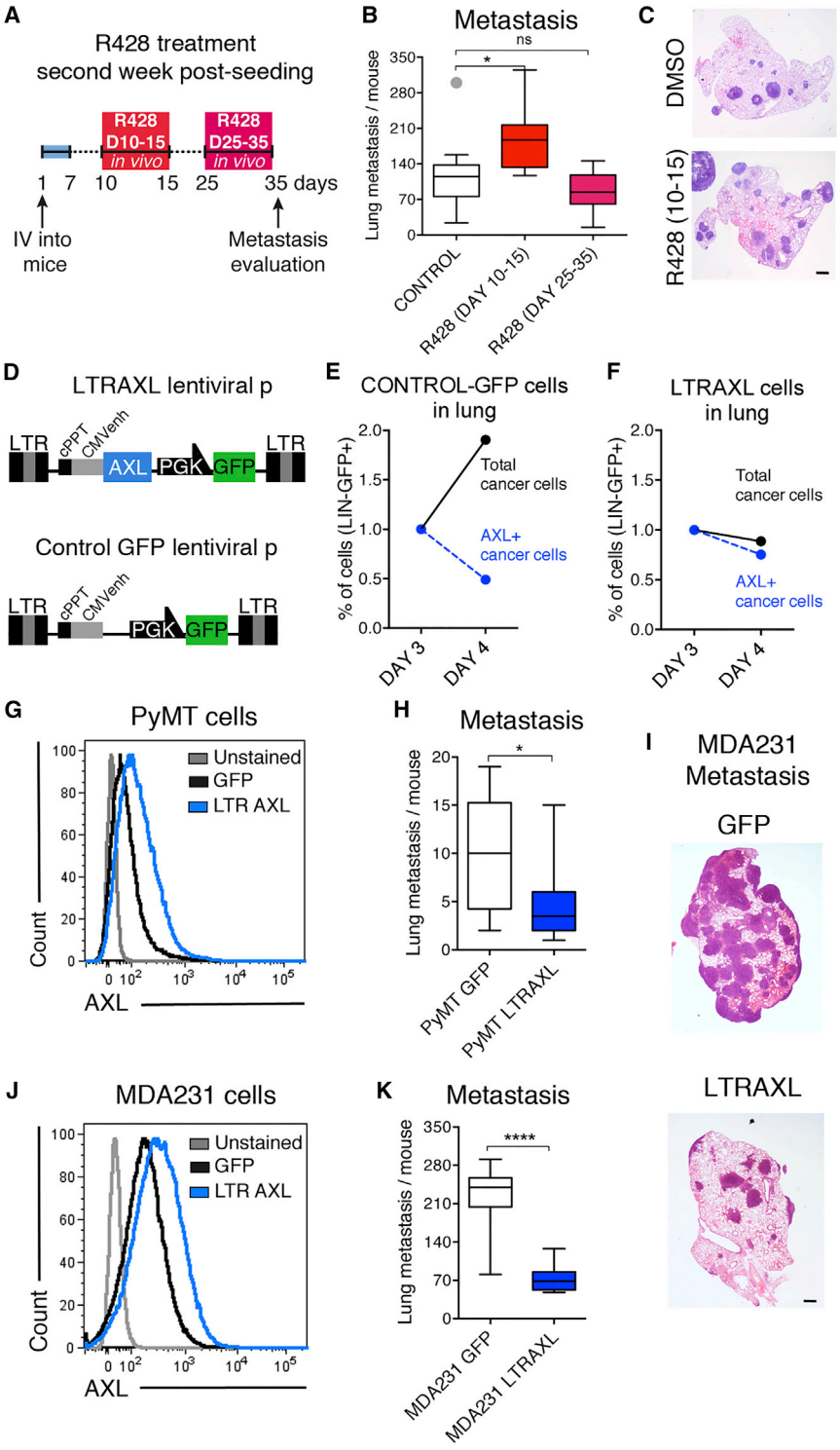

Figure 7. EMT-Stabilized Cells Do Not Metastasize Efficiently

(A) Schematic showing the R428 treatment setting.

(B) Box plot displaying the metastatic burden of mice injected with primary PyMT cells for the indicated groups: DMSO, n = 11; R428, days 10–15, n = 10; and R428, days 25–35, n = 7. The superficial lung metastasis number was evaluated.

(C) Representative images of the indicated lung sections. Scale bar, 100 μm.

(D) Schematic of the LTR-driven lentiviral plasmid expressing the human *Axl* open reading frame (ORF) (top) and control plasmid (bottom).

(E and F) Flow cytometry analysis showing the percentage of total cancer cells (black) and AXL$^+$ cells (blue) in the lung 3 or 4 days after intravenous injection of MDA231 expressing the control-GFP construct (E) or LTR-AXL construct (F). Data are displayed as the group average relative to day 3 (n = 4–6/group).

(G) Representative flow cytometry plot showing the expression levels of AXL in the indicated primary PyMT cells.

(H) Box plot showing superficial lung metastasis quantification after intravenous injection of PyMT cells expressing control-GFP or LTR-AXL constructs (n = 10/group).

(I) Representative H&E staining of lung sections of mice injected with MDA231 of the indicated groups. Scale bar, 100 μm.

(J) Representative flow cytometry plot showing the expression levels of AXL in the indicated MDA231 cells.

(K) Box plot showing the superficial metastasis quantification after intravenous injection of MDA231 cells expressing the control-GFP or LTR-AXL constructs (n = 8/group).

Error bars represent SEM. *p < 0.05, ****p < 0.0001.

colonization (Figure 7). Indeed, prolonged *Axl* gene activation in cancer cells strongly reduces metastatic ability (Figures 7H and 7K). AXL expression in the context of breast cancer lung metastasis opposes primary tumor initiation (Figures 7G–7K and S7D), likely because of differences in the requirement of its tyrosine kinase receptor function, which is also crucial for other cancer types (Ben-Batalla et al., 2013).

Remarkably, we provide experimental evidence that epithelial plasticity is mediated by crosstalk between the cancer cell and stroma (Figure 6). During the second colonization phase, the newly activated fibroblasts generated during the first phase induce a phenotype switch in MICs. BMP-dependent ID1 activation in cancer cells is triggered by exposure to CaCM (Figures 6L and 6M). This effect, observed in vitro, is corroborated in vivo by the enhancement of pSMAD1-5 activity and downmodulation of TGF-β signaling in favor of an ID1-positive proliferative state. Indeed, treatment of mice with the specific BMP inhibitor LDN193189 during the second colonization phase inhibits metastasis (Figures 6N and 6O).

Overall, this study provides a refined definition of distant colonization by more mesenchymal cancer cells where their

niche-activation capacity is linked to their mesenchymal status and THBS2 secretion. Subsequently, activated fibroblasts drive MICs to revert to a more epithelial phenotype. This model highlights the importance of cancer cell-stroma crosstalk in modulating the optimal phenotype for cancer cells during the dynamic metastatic process.

EXPERIMENTAL PROCEDURES

Statistical Analysis

Statistical analyses were performed using Prism software (GraphPad Software). p values were obtained from two-tailed Student's t tests with paired or unpaired adjustment. One-column t test was used for comparisons with a normalized value. One-tailed t test was used for Figure 4E. Where indicated, two-way ANOVA was used to perform multiple comparisons or multiple variables analysis between experimental groups. Significance was set at $p < 0.05$. Graphs show the symbols describing the p value (*$p < 0.05$, **$p < 0.01$, ***$p < 0.001$, ****$p < 0.0001$).

Animal Procedures

All experimental procedures involving mice were performed in accordance with United Kingdom regulations under project license PPL 80/2531. Further information can be found in the Supplemental Experimental Procedures.

ImageStream Analysis

Lungs or Matrigel collagen gels from co-culture experiments were digested and dissociated to obtain a single-cell suspension, stained with a live/dead fixable dye, fixed, and stained with the indicated primary antibodies (antibody descriptions and working dilutions can be found in Table S4 and in the Supplemental Experimental Procedures). Tumor cells in the lung were identified by GFP expression. The acquired ImageStream data were analyzed using Amnis IDEA management software.

ACCESSION NUMBERS

The accession number for the microarray data reported in this paper is GEO: GSE63558.

SUPPLEMENTAL INFORMATION

Supplemental Information includes Supplemental Experimental Procedures, seven figures, and four tables and can be found with this article online at http://dx.doi.org/10.1016/j.celrep.2015.11.025.

AUTHOR CONTRIBUTIONS

Y.P.M. designed and performed most of the experiments, analyzed data, and contributed to manuscript preparation. D.P. designed and performed the invasion experiments and analyzed data. A.R performed pSMAD1-5 and ID1 detection in vitro and analyzed data. L.O. and F.C. performed pilot experiments and contributed to discussions. P.C. performed the bioinformatics analysis. B.S.D. performed staining of the lung sections. S.D. provided critical reagents. C.H. and E.S. designed and supervised some experiments, provided crucial conceptual advice, and revised the manuscript. I.M. designed and supervised the study, interpreted data, and wrote the manuscript.

ACKNOWLEDGMENTS

We thank the members of the Tumour Host Interaction Laboratory (THI) and Tumour Cell Biology Lab (TCB) at the Crick Institute for support and discussions. Particularly, we thank Dr. Laurie Gay, Stefanie Wculek (THI), and Dr. Marco Montagner (TCB) for critically reading the manuscript. We are thankful to Robert Moore from the THI, Emma Nye from the Experimental Histopathology unit, Julie Bee from the Biological Resources unit, and all members of the FACS laboratory at Crick Institute for invaluable technical help. We thank Dr. Levi A. Garraway from the Broad Institute of Harvard and Dr. Paul Bornstein from the Biochemistry and Medicine Department, University of Washington, for sharing, through Addgene, the pDONR223-AXL and pcDNA3-mTHBS2 plasmids, respectively.

Received: November 28, 2014
Revised: October 5, 2015
Accepted: November 4, 2015
Published: December 3, 2015

REFERENCES

Aceto, N., Bardia, A., Miyamoto, D.T., Donaldson, M.C., Wittner, B.S., Spencer, J.A., Yu, M., Pely, A., Engstrom, A., Zhu, H., et al. (2014). Circulating tumor cell clusters are oligoclonal precursors of breast cancer metastasis. Cell *158*, 1110–1122.

Ben-Batalla, I., Schultze, A., Wroblewski, M., Erdmann, R., Heuser, M., Waizenegger, J.S., Riecken, K., Binder, M., Schewe, D., Sawall, S., et al. (2013). Axl, a prognostic and therapeutic target in acute myeloid leukemia mediates paracrine crosstalk of leukemia cells with bone marrow stroma. Blood *122*, 2443–2452.

Brabletz, T. (2012). EMT and MET in metastasis: where are the cancer stem cells? Cancer Cell *22*, 699–701.

Calvo, F., Ege, N., Grande-Garcia, A., Hooper, S., Jenkins, R.P., Chaudhry, S.I., Harrington, K., Williamson, P., Moeendarbary, E., Charras, G., and Sahai, E. (2013). Mechanotransduction and YAP-dependent matrix remodelling is required for the generation and maintenance of cancer-associated fibroblasts. Nat. Cell Biol. *15*, 637–646.

Chen, J., Li, Y., Yu, T.-S., McKay, R.M., Burns, D.K., Kernie, S.G., and Parada, L.F. (2012). A restricted cell population propagates glioblastoma growth after chemotherapy. Nature *488*, 522–526.

Diepenbruck, M., Waldmeier, L., Ivanek, R., Berninger, P., Arnold, P., van Nimwegen, E., and Christofori, G. (2014). Tead2 expression levels control the subcellular distribution of Yap and Taz, zyxin expression and epithelial-mesenchymal transition. J. Cell Sci. *127*, 1523–1536.

Gaggioli, C., Hooper, S., Hidalgo-Carcedo, C., Grosse, R., Marshall, J.F., Harrington, K., and Sahai, E. (2007). Fibroblast-led collective invasion of carcinoma cells with differing roles for RhoGTPases in leading and following cells. Nat. Cell Biol. *9*, 1392–1400.

Giampieri, S., Manning, C., Hooper, S., Jones, L., Hill, C.S., and Sahai, E. (2009). Localized and reversible TGF-β signalling switches breast cancer cells from cohesive to single cell motility. Nat. Cell Biol. *11*, 1287–1296.

Gjerdrum, C., Tiron, C., Høiby, T., Stefansson, I., Haugen, H., Sandal, T., Collett, K., Li, S., McCormack, E., Gjertsen, B.T., et al. (2010). Axl is an essential epithelial-to-mesenchymal transition-induced regulator of breast cancer metastasis and patient survival. Proc. Natl. Acad. Sci. USA *107*, 1124–1129.

Gupta, G.P., Perk, J., Acharyya, S., de Candia, P., Mittal, V., Todorova-Manova, K., Gerald, W.L., Brogi, E., Benezra, R., and Massagué, J. (2007). ID genes mediate tumor reinitiation during breast cancer lung metastasis. Proc. Natl. Acad. Sci. USA *104*, 19506–19511.

Hermann, P.C., Huber, S.L., Herrler, T., Aicher, A., Ellwart, J.W., Guba, M., Bruns, C.J., and Heeschen, C. (2007). Distinct populations of cancer stem cells determine tumor growth and metastatic activity in human pancreatic cancer. Cell Stem Cell *1*, 313–323.

Holland, S.J., Pan, A., Franci, C., Hu, Y., Chang, B., Li, W., Duan, M., Torneros, A., Yu, J., Heckrodt, T.J., et al. (2010). R428, a selective small molecule inhibitor of Axl kinase, blocks tumor spread and prolongs survival in models of metastatic breast cancer. Cancer Res. *70*, 1544–1554.

Kim, H., Watkinson, J., Varadan, V., and Anastassiou, D. (2010). Multi-cancer computational analysis reveals invasion-associated variant of desmoplastic reaction involving INHBA, THBS2 and COL11A1. BMC Med. Genomics *3*, 51.

Liu, J.C., Deng, T., Lehal, R.S., Kim, J., and Zacksenhaus, E. (2007). Identification of tumorsphere- and tumor-initiating cells in HER2/Neu-induced mammary tumors. Cancer Res. *67*, 8671–8681.

Malanchi, I. (2013). Tumour cells coerce host tissue to cancer spread. Bonekey Rep. *2*, 371.

Malanchi, I., Peinado, H., Kassen, D., Hussenet, T., Metzger, D., Chambon, P., Huber, M., Hohl, D., Cano, A., Birchmeier, W., and Huelsken, J. (2008). Cutaneous cancer stem cell maintenance is dependent on beta-catenin signalling. Nature *452*, 650–653.

Malanchi, I., Santamaria-Martínez, A., Susanto, E., Peng, H., Lehr, H.-A., Delaloye, J.-F., and Huelsken, J. (2012). Interactions between cancer stem cells and their niche govern metastatic colonization. Nature *481*, 85–89.

Mani, S.A., Guo, W., Liao, M.-J., Eaton, E.N., Ayyanan, A., Zhou, A.Y., Brooks, M., Reinhard, F., Zhang, C.C., Shipitsin, M., et al. (2008). The epithelial-mesenchymal transition generates cells with properties of stem cells. Cell *133*, 704–715.

Massagué, J. (2008). TGFbeta in Cancer. Cell *134*, 215–230.

Morel, A.-P., Lièvre, M., Thomas, C., Hinkal, G., Ansieau, S., and Puisieux, A. (2008). Generation of breast cancer stem cells through epithelial-mesenchymal transition. PLoS ONE *3*, e2888.

Nguyen, D.X., Chiang, A.C., Zhang, X.H.-F., Kim, J.Y., Kris, M.G., Ladanyi, M., Gerald, W.L., and Massagué, J. (2009). WNT/TCF signaling through LEF1 and HOXB9 mediates lung adenocarcinoma metastasis. Cell *138*, 51–62.

Nieto, M.A. (2013). Epithelial plasticity: a common theme in embryonic and cancer cells. Science *342*, 1234850.

Ombrato, L., and Malanchi, I. (2014). The EMT universe: space between cancer cell dissemination and metastasis initiation. Crit. Rev. Oncog. *19*, 349–361.

Oskarsson, T., Acharyya, S., Zhang, X.H.-F., Vanharanta, S., Tavazoie, S.F., Morris, P.G., Downey, R.J., Manova-Todorova, K., Brogi, E., and Massagué, J. (2011). Breast cancer cells produce tenascin C as a metastatic niche component to colonize the lungs. Nat. Med. *17*, 867–874.

Paccez, J.D., Vogelsang, M., Parker, M.I., and Zerbini, L.F. (2014). The receptor tyrosine kinase Axl in cancer: biological functions and therapeutic implications. Int. J. Cancer *134*, 1024–1033.

Padua, D., Zhang, X.H.-F., Wang, Q., Nadal, C., Gerald, W.L., Gomis, R.R., and Massagué, J. (2008). TGFbeta primes breast tumors for lung metastasis seeding through angiopoietin-like 4. Cell *133*, 66–77.

Peinado, H., Olmeda, D., and Cano, A. (2007). Snail, Zeb and bHLH factors in tumour progression: an alliance against the epithelial phenotype? Nat. Rev. Cancer *7*, 415–428.

Qian, B.-Z., Li, J., Zhang, H., Kitamura, T., Zhang, J., Campion, L.R., Kaiser, E.A., Snyder, L.A., and Pollard, J.W. (2011). CCL2 recruits inflammatory monocytes to facilitate breast-tumour metastasis. Nature *475*, 222–225.

Reya, T., and Clevers, H. (2005). Wnt signalling in stem cells and cancer. Nature *434*, 843–850.

Sheridan, C. (2013). First Axl inhibitor enters clinical trials. Nat. Biotechnol. *31*, 775–776.

Sleeman, J.P. (2012). The metastatic niche and stromal progression. Cancer Metastasis Rev. *31*, 429–440.

Thiery, J.P., Acloque, H., Huang, R.Y.J., and Nieto, M.A. (2009). Epithelial-mesenchymal transitions in development and disease. Cell *139*, 871–890.

Tichet, M., Prod'Homme, V., Fenouille, N., Ambrosetti, D., Mallavialle, A., Cerezo, M., Ohanna, M., Audebert, S., Rocchi, S., Giacchero, D., et al. (2015). Tumour-derived SPARC drives vascular permeability and extravasation through endothelial VCAM1 signalling to promote metastasis. Nat. Commun. *6*, 6993.

Tsai, J.H., Donaher, J.L., Murphy, D.A., Chau, S., and Yang, J. (2012). Spatiotemporal regulation of epithelial-mesenchymal transition is essential for squamous cell carcinoma metastasis. Cancer Cell *22*, 725–736.

Vermeulen, L., De Sousa E Melo, F., van der Heijden, M., Cameron, K., de Jong, J.H., Borovski, T., Tuynman, J.B., Todaro, M., Merz, C., Rodermond, H., et al. (2010). Wnt activity defines colon cancer stem cells and is regulated by the microenvironment. Nat. Cell Biol. *12*, 468–476.

Vuoriluoto, K., Haugen, H., Kiviluoto, S., Mpindi, J.-P., Nevo, J., Gjerdrum, C., Tiron, C., Lorens, J.B., and Ivaska, J. (2011). Vimentin regulates EMT induction by Slug and oncogenic H-Ras and migration by governing Axl expression in breast cancer. Oncogene *30*, 1436–1448.

Wellner, U., Schubert, J., Burk, U.C., Schmalhofer, O., Zhu, F., Sonntag, A., Waldvogel, B., Vannier, C., Darling, D., zur Hausen, A., et al. (2009). The EMT-activator ZEB1 promotes tumorigenicity by repressing stemness-inhibiting microRNAs. Nat. Cell Biol. *11*, 1487–1495.

Yu, Y., Xiao, C.-H., Tan, L.-D., Wang, Q.-S., Li, X.-Q., and Feng, Y.-M. (2014). Cancer-associated fibroblasts induce epithelial-mesenchymal transition of breast cancer cells through paracrine TGF-β signalling. Br. J. Cancer *110*, 724–732.

Cell Reports

Supplemental Information

Mesenchymal Cancer Cell-Stroma Crosstalk Promotes Niche Activation, Epithelial Reversion, and Metastatic Colonization

Yaiza del Pozo Martin, Danielle Park, Anassuya Ramachandran, Luigi Ombrato, Fernando Calvo, Probir Chakravarty, Bradley Spencer-Dene, Stefanie Derzsi, Caroline S. Hill, Erik Sahai, and Ilaria Malanchi

Supplemental Information

- **Supplemental Figures**

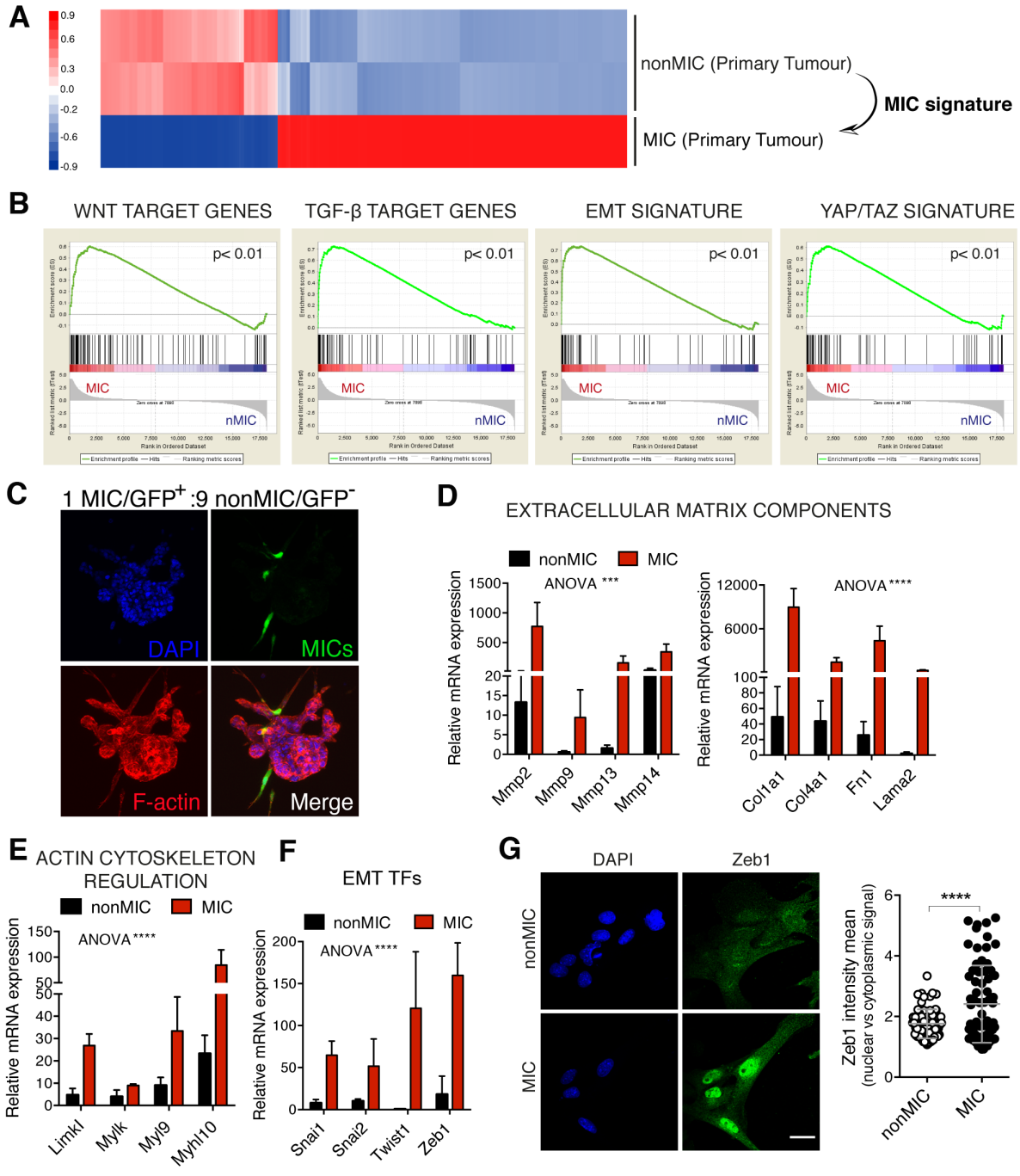

Figure S1 (relates to Figure 1). MICs are in a highly secretory mesenchymal state

(A) Heatmap represents the gene expression profile of MICs and nonMICs isolated from MMTV-PyMT primary tumors. The MIC signature includes all differently expressed genes in MICs compared to nonMICs (GEO:GSE63558). (B) Gene Set Enrichment Analysis (GSEA) plots show the correlation of the MIC signature with WNT and TGF-β target genes, and an EMT and YAP/TAZ signature (detailed information and references for each signature can be found in the Supplemental Experimental Procedures). (C) Images show a mixed spheroid stained with DAPI (blue) and F-actin (red). MICs from actin-GFP/PyMT tumors and nonMICs from non-labeled PyMT tumors were freshly isolated by cell sorting and re-aggregated overnight in suspension in a 1:9 MIC:nonMIC ratio mimicking the *in vivo* frequency of both populations. Note the invasive MIC cells identified by GFP (green) (quantification in Figure 1E). (D-F) Quantitative real time PCR analysis compares the gene expression levels of extracellular matrix components (D), actin cytoskeleton regulatory molecules (E) and EMT transcription factors (F) in MICs and nonMICs freshly isolated from three primary tumors. Data from 3 different experiments performed in triplicate (normalized to *Gapdh*). Bars represent mean ± sem. $p<0.0001$ by ANOVA comparing the MIC *versus* nonMIC gene sets in each plot. (G) Representative images show Zeb1 staining (green) and nuclear DAPI staining (blue) in sorted MICs and nonMICs. Cells were stained 24h after isolation and plating. Scale bar, 20 μm. Chart indicates the level of nuclear *versus* cytoplasmic intensity mean of Zeb1 (mean ± SD of the population). Data from one representative experiment out of 2 are shown.

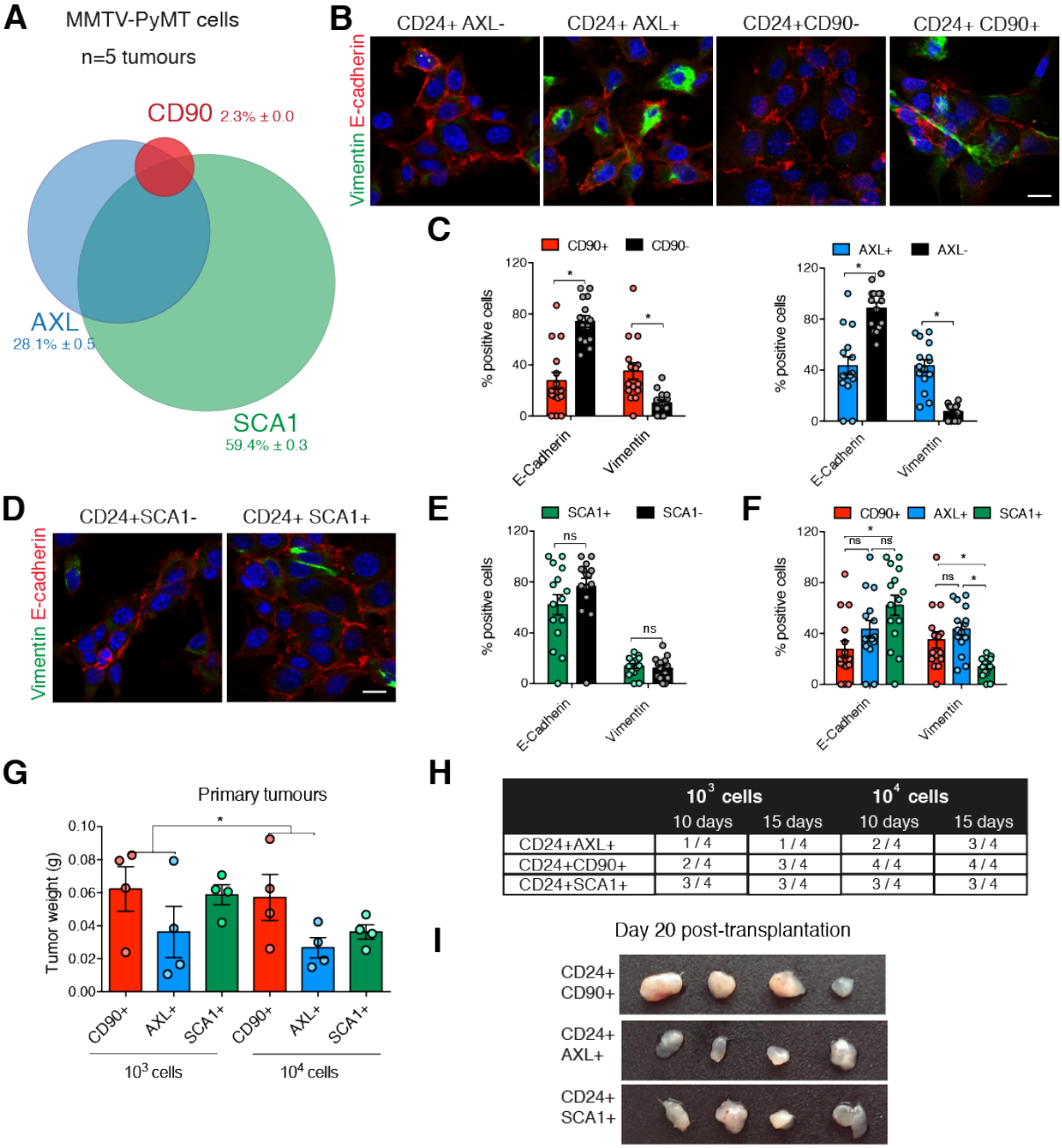

	10^3 cells		10^4 cells	
	10 days	15 days	10 days	15 days
CD24+AXL+	1 / 4	1 / 4	2 / 4	3 / 4
CD24+CD90+	2 / 4	3 / 4	4 / 4	4 / 4
CD24+SCA1+	3 / 4	3 / 4	3 / 4	3 / 4

Figure S2 (relates to Figure 1). MICs are in a mesenchymal state defined by AXL expression

(A) Venn diagram illustrates the relationship between the different PyMT populations and their relative frequency in PyMT tumors measured by FACS. MICs ($CD24^+CD90^+$) are represented in red, $CD24^+AXL^+$ in blue and $CD24^+SCA1^+$ in green. Mean ± sem for each population is indicated (n=5 tumors). (B) Representative pictures show E-Cadherin and

Vimentin expression in MICs ($CD24^+CD90^+$) and $CD24^+AXL^+$. Cells were isolated by cell sorting from the same primary tumor and plated overnight on collagen-coated dishes prior to analysis. Scale bar, 15 µm. (C) Histograms indicate the percentage (mean ± sem) of E-Cadherin and Vimentin positive cells in MICs ($CD24^+CD90^+$) and $CD24^+AXL^+$ cells per field of view (representative pictures in B). Data from one representative experiment from a total of two are shown. (D) Representative pictures show E-Cadherin and Vimentin expression in the $CD24^+SCA1^+$ population of PyMT cells. Cells were isolated and analyzed as in (B). Scale bar, 15 µm. (E) Histogram indicates the percentage (mean ± sem) of E-Cadherin and Vimentin positive cells in the $CD24^+SCA1^+$ population per field of view (representative pictures in D). Data from one representative experiment of two are shown. (F) Plot displays together the percentage of E-Cadherin and Vimentin positive cells in the different PyMT populations evaluated in C and E. (G) Bar graph shows the weight (grams) of primary tumor formed by MICs, $CD24^+AXL^+$ and $CD24^+SCA1^+$ populations. Cells were sorted in the different pools from the same primary tumor cell preparation after overnight plating on collagen-I coated dishes. Either 10^3 cells or 10^4 cells from each population were orthotopically transplanted into mice and tumor growth was evaluated 30 and 20 days post-transplantation, respectively (n=4, number of tumors). (H) Table indicates the tumor initiation development over time of the indicated cell subpools after orthotopic transplantation (as in G). (I) Representative images of the tumors grown as specified in G, harvested 20 days post-transplantation of 10^4 cells.

A

MIC secreted factors	Fold change (MIC vs nonMIC)
THBS2	27.93
CCL7	10.41
CCL11	6.42
ANGTL4	5.59
CXCL10	1.83
CYR61	1.62
WNT5A	1.45

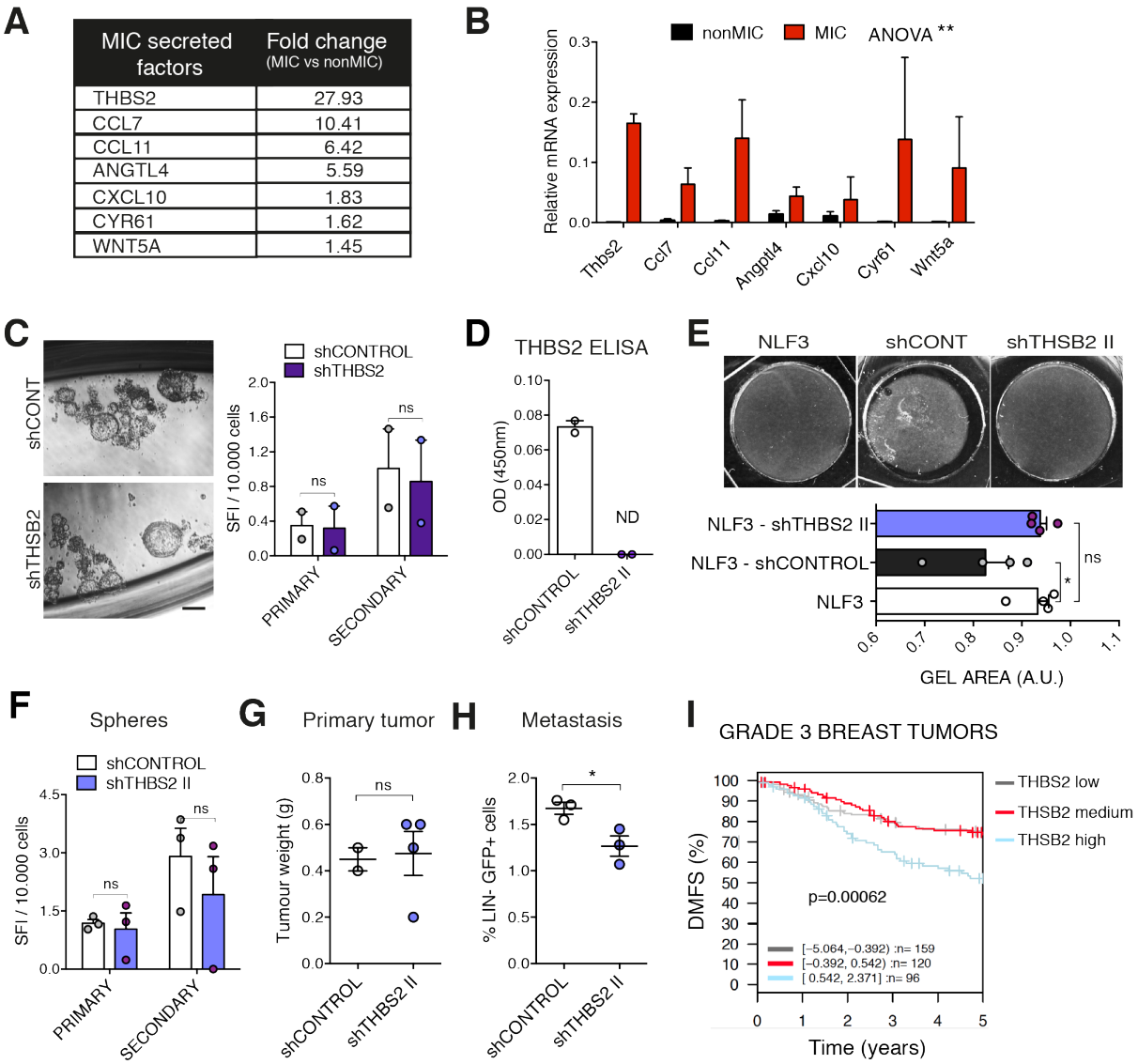

Figure S3 (relates to Figure 3). THBS2 expression in MICs and *Thbs2* knockdown characterization in primary PyMT cells

(A) List of selected top secreted factors from the MIC signature in Figure S1A. Fold change expression of each factor obtained by comparing MIC *versus* nonMIC signatures. (B) Quantitative real time PCR analysis shows the expression levels of the secreted factors in MICs *versus* nonMICs. Data from 3 different tumors performed in triplicate (normalized to *Gapdh*). Bar represent mean ± sem. p=0.0057 by ANOVA comparing the gene set in MIC *versus* nonMIC. (C) (Left) Images show representative

pictures of spheres formed by PyMT cells expressing shCONTROL and shTHBS2 I lentiviral constructs in suspension. Spheres were quantified 7 days after plating a single PyMT cell suspension (primary) and 7 days after passage (secondary). Scale bar, 200 µm. (Right) Histogram shows the mean ± sem of the SFI (Sphere Formation Index) of 2 independent experiments. (D) Histogram shows the relative levels of secreted THBS2 measured by ELISA in media conditioned by PyMT cells expressing shCONTROL or shTHBS2 II lentiviral constructs. Data from 2 experiments performed in duplicate. Bars represent mean ± sem. (E) (Upper panel) Images show gel contraction by normal lung fibroblasts (NLF3) co-culture with or without primary PyMT cells expressing shCONTROL or shTHBS2 II lentiviral constructs. (Lower panel) Histogram shows the mean ± sem of the gel area in arbitrary units (n=4, number of gels per group). (F) Sphere formation assay by PyMT cells expressing shCONTROL and shTHBS2 II lentiviral constructs in suspension (as described in C). Histogram shows the mean ± sem of the SFI (Sphere Formation Index) of 3 independent experiments. (G) Early primary tumor growth of PyMT cells expressing shCONTROL or shTHBS2 II lentiviral constructs in a collective cell challenge. Middle line represents the mean, and horizontal lines the minimum and maximum value (n= mice per group: shCONTROL, 2; shTHBS2 II, 4). (H) Metastatic potential of total PyMT cells in the lung expressing shCONTROL or shTHBS2 II lentiviral constructs 5 weeks after intravenous injection assessed by flow cytometry quantification of total GFP^+ cells in the lung. Middle line represents the mean, and horizontal lines the minimum and maximum value (n=3 mice per group). (I) Kaplan-Meier plot shows the prognostic value of THBS2 in high-grade breast carcinoma represented as Distant Metastasis-Free Survival (DMFS) of grade 3 breast cancer patients classified

according to *Thbs2* expression levels. Data from Gene expression-based Outcome for Breast cancer Online (GOBO) database.

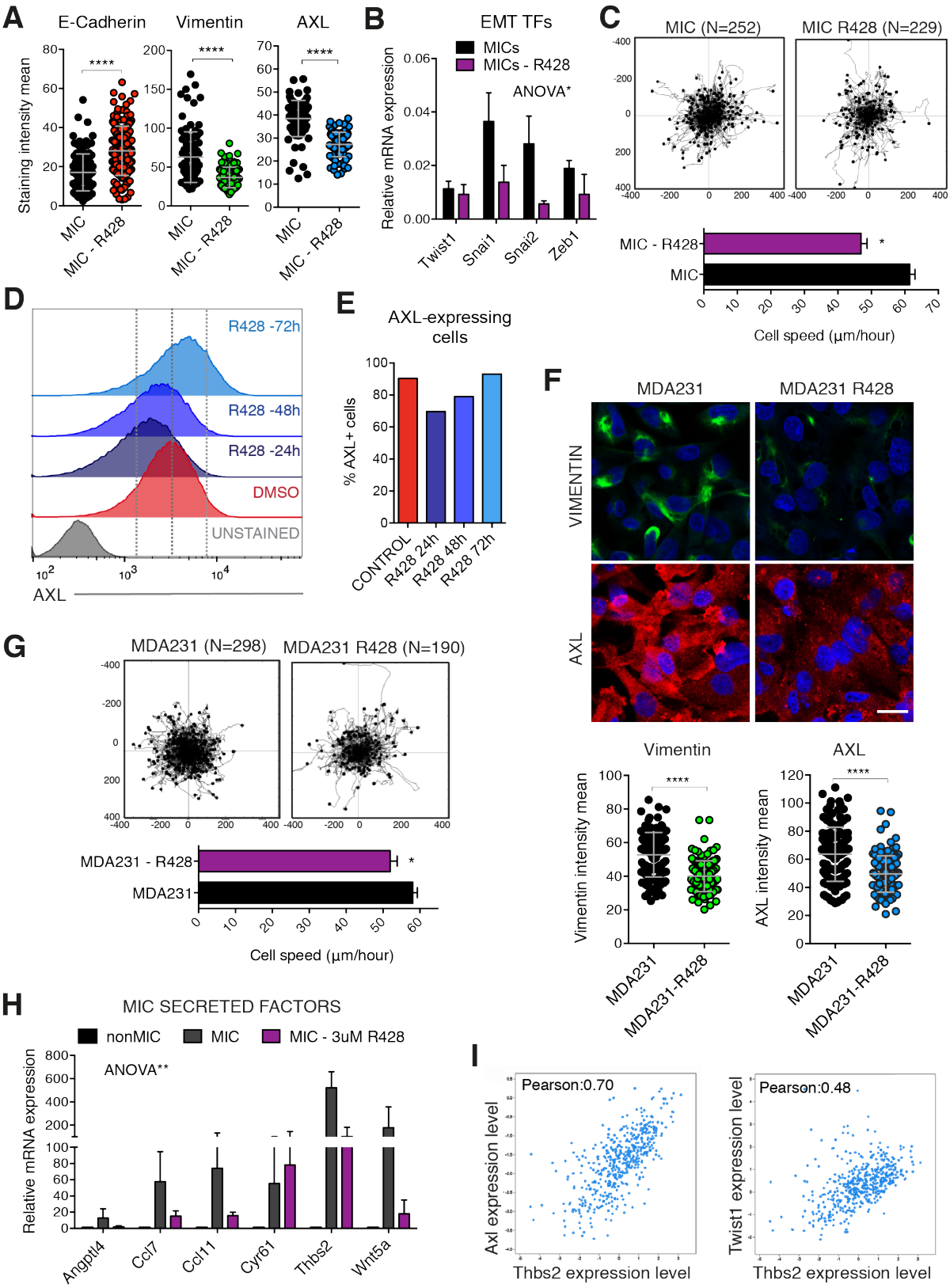
A
E-Cadherin
Vimentin
AXL
Staining intensity mean
****
MIC
MIC - R428
B
EMT TFs
MICs
MICs - R428
ANOVA*
Relative mRNA expression
Twist1
Snai1
Snai2
Zeb1
C
MIC (N=252)
MIC R428 (N=229)
MIC - R428
MIC
*
Cell speed (µm/hour)
D
R428 -72h
R428 -48h
R428 -24h
DMSO
UNSTAINED
AXL
E
AXL-expressing cells
% AXL+ cells
CONTROL
R428 24h
R428 48h
R428 72h
F
MDA231
MDA231 R428
VIMENTIN
AXL
Vimentin
AXL
Vimentin intensity mean
AXL intensity mean
MDA231
MDA231-R428
G
MDA231 (N=298)
MDA231 R428 (N=190)
MDA231 - R428
MDA231
Cell speed (µm/hour)
H
MIC SECRETED FACTORS
nonMIC
MIC
MIC - 3uM R428
ANOVA**
Relative mRNA expression
Angptl4
Ccl7
Ccl11
Cyr61
Thbs2
Wnt5a
I
Pearson:0.70
Axl expression level
Thbs2 expression level
Pearson:0.48
Twist1 expression level
Thbs2 expression level

Figure S4 (relates to Figure 4). Effects of R428 AXL inhibitor on cancer cells mesenchymal state

(A) Charts show the quantification of the expression levels of E-Cadherin, Vimentin and AXL in sorted MICs cultured overnight in collagen-I coated dishes and treated 24h before analysis with DMSO or 1.5 μM R428 for 3h. Data from one representative of three experiments are shown. Error bars indicate mean ± SD of the population (see Figure 4A for representative pictures). (B) Quantitative real time PCR analysis compares the gene expression levels of different EMT transcription factors in MICs 24h after treatment with DMSO or 1.5 μM R428 for 3h. Data from 3 different experiments performed in triplicate (normalized to *Gapdh*). Error bars represent mean ± sem. p=0.0308 by ANOVA comparing the gene set in MICs *versus* MICs-R428. (C) Rose plots show the tracking path of MICs 24h after treatment with DMSO or 1.5 μM R428 for 3h. Histogram shows the mean ± sem of the cell speed quantified in 2 independent experiments. (D) Flow cytometry histograms show the expression levels of AXL in the MDA231 cell line 24h, 48h or 72h after treatment with 3 μM R428. (E) Flow cytometry analysis of the percentage of AXL^+ cells in the MDA231 cell line 24h, 48h or 72h after treatment with 3 μM R428. (F) Representative immunofluorescence images show the expression levels of Vimentin and AXL in MDA231 cells 24h after treatment with DMSO or 3 μM R428 for 3h. Charts indicate the quantification of expression levels of Vimentin (left) and AXL (right) in the above-indicated conditions. Data from one representative experiment from of two are shown. Line and error bar indicate mean ± SD of the population. (G) Rose plots show the tracking path of MDA231 cells 24h after treatment with DMSO or 3 μM R428 for 3h. Histogram

shows the mean ± sem of the cell speed quantified in 2 independent experiments. (H) Quantitative real time PCR analysis compares the gene expression levels of selected secreted factors in nonMICs and MICs isolated from primary tumors and treated 24h before analysis with DMSO or 1.5 μM R428 for 3h. Data from 3 different experiments performed in triplicate (normalized to *Gapdh*). Bar represent mean ± sem. p=0.0041 by ANOVA comparing the gene set in MICs *versus* MICs-R428. (I) Plots show the correlation between *Thbs2* gene expression and *Axl,* or *Twist1* expression in human invasive breast carcinoma biopsy samples. Data sets and analysis can be found at cBioPortal for Cancer Genomics (www.cbioportal.org). Further details are provided in the Supplemental Experimental Procedures.

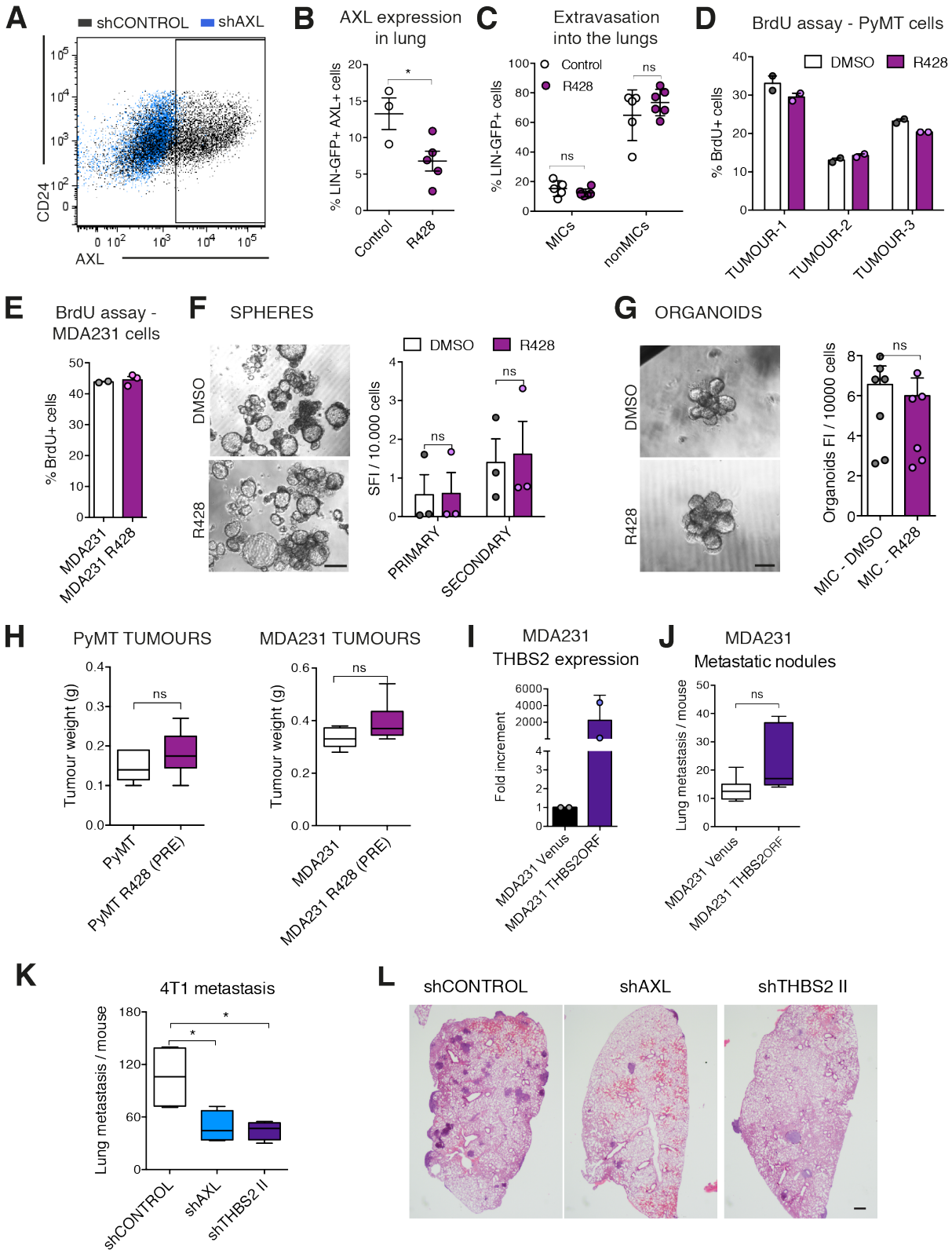

Figure S5 (relates to Figure 5). Effects of THBS2 and AXL altered levels in tumor cell behavior

(A) Flow cytometry dot plot overlaid shows AXL expression in primary PyMT cells expressing shCONTROL (black dots) and shAXL (blue dots) lentiviral constructs. (B) Flow cytometry analysis of AXL^+ cancer cells in the lung after R428 treatment *in vivo*. Mice were intravenously injected with primary PyMT GFP^+ cells and treated daily with DMSO (vehicle) or R428 (12.5 mg/kg) for 3 days, when lungs were extracted for analysis. Chart shows mean ± sem (n=3-5 per group). (C) Flow cytometry analysis to assess MICs and nonMICs cell extravasation into the lung after R428 pre-treatment *in vitro*. PyMT/GFP^+ cells were treated 24 hours prior to intravenous injection into mice with DMSO or 1.5 μM R428 *in vitro.* Flow cytometry analysis was performed 24h post-injection after lung perfusion. Chart displays the mean ± sem (n=5-6 per group). (D) Flow cytometry analysis shows BrdU incorporation over a 3 hours pulse by primary PyMT cells 24h after treatment with DMSO or 1.5 μM R428 for 3h. Data collected from 3 different tumors preparations performed in duplicate. (E) Flow cytometry analysis shows BrdU incorporation over a 3 hours pulse by MDA231 cells 24h after treatment with DMSO or 3 μM R428 for 3h. Histogram shows mean ± sem of 2-3 MDA231 cancer cell line preparations. (F) Sphere culture assay. (Left) Images show representative pictures of spheres formed by primary PyMT cells 7 days after pre-treatment with DMSO or 1.5 μM R428. Scale bar, 200 μm. (Right) Histogram shows mean ± sem of 3 independent experiments. Spheres were quantified 7 days after plating a single PyMT suspension (primary) and 7 days after passage (secondary). (G) Organoid assay. Images show representative pictures of organoids formed by primary PyMT cells embedded in Matrigel 7 days after pre-treatment with DMSO or 1.5 μM R428. Scale bar, 200 μm. Histogram shows the mean ± sem of the wells (n=3-4) assessed in 2 independent experiments. (H) Box plot displays tumor burden evaluated 3 weeks after engraftment of

PyMT cells (left) or MDA231 cells (right) pre-treated with DMSO or 1.5 μM R428 (PyMT) or 3 μM R428 (MDA231) (n=6, mice per group). (I) Quantitative real time PCR analysis shows *Thbs2* gene expression levels in MDA231 cells expressing Venus (control) or THBS2ORF lentiviral constructs (normalised to *Gapdh*). Data show technical duplicates. (J) Box plot shows the metastatic burden after intravenous injection of MDA231 cells expressing VENUS or THBS2ORF lentiviral constructs (n=5-7 mice per group). Micrometastasis were evaluated in lung histological sections (rest of the experiment is displayed in Figure 5G). (K) Box plot shows the metastatic burden after intravenous injection of 4T1 cell line expressing shCONTROL, shAXL or shTHBS2 lentiviral constructs (n=4, mice per group). Number of superficial lung metastasis was evaluated. (L) Representative images of lung sections stained with Hematoxylin and Eosin from (K). Scale bar, 100 μm.

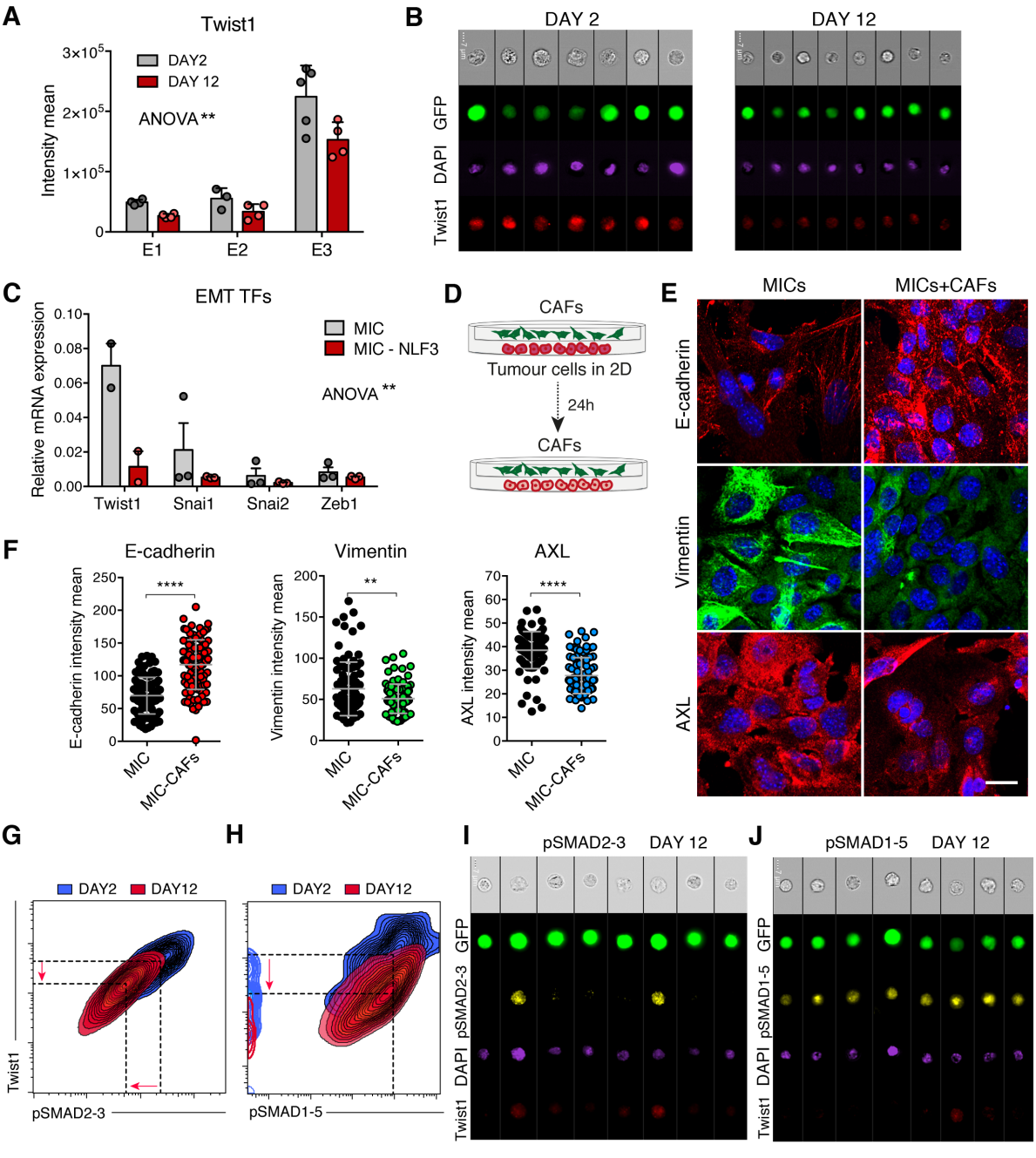

Figure S6 (relates to Figure 6). *In vivo* and *in vitro* mesenchymal cancer cells phenotypic modulations

(A) Bar graph shows the intensity mean of Twist1 in $CD24^{+}AXL^{+}$ cells in the lung in a metastasis time course analyzed by ImageStream. Data from three independent experiments are shown (n=3-5, mice per group). P value determined comparing the

differences in Twist1 intensity at day 2 and day 12 of metastasis across the three experiments by ANOVA. (B) Representative ImageStream images show GFP^+ cells (green) isolated from metastatic lungs injected with $CD24^+AXL^+$ tumor cells 2 or 12 days prior to analysis stained for nuclear DAPI (blue) and Twist1 (red); intensity quantification in A. (C) Quantitative real time PCR analysis compares the gene expression levels of different EMT transcription factors in MICs co-cultured with or without NLF3 as in Figure 2E. Data from 2-3 different experiments performed in triplicate (normalized to *Gapdh*). Error bars represent mean ± sem. p=0.0018 by ANOVA comparing the gene set in MICs *versus* MICs-NLF3. (D) Schematic shows the co-culture setting where MICs are seeded in adherent condition on collagen-I coated dishes in the lower compartment and CAFs in the upper chamber for 24h. (E) Representative images show the expression of E-Cadherin, Vimentin and AXL in MICs co-cultured with or without CAFs for 24 hours as in D. Scale bar, 20 μm. (F) Charts indicate the expression levels of E-Cadherin, AXL and Vimentin in MICs co-cultured with or without CAFs for 24 hours. Data from one representative experiment of two are shown. Line and error bar indicate mean ± SD of the population. (G-H) Flow cytometry contour plots generated by ImageStream show the overall intensity of Twist1 *versus* pSMAD1-5 (G) or pSMAD2-3 (H) in $CD24^+AXL^+$ tumor cells in the lung 2 days (blue) and 12 days (red) post intravenous injection. Note the overall decrease in Twist1 and pSMAD2-3 staining intensity while pSMAD1-5 is maintained. (I-J) Representative ImageStream images show GFP^+ cells (green) isolated from metastatic lungs injected with $CD24^+AXL^+$ tumor cells 12 days prior to analysis stained for nuclear DAPI (blue) and pSMAD2-3 (yellow) and Twist1 (red) (I) or pSMAD1-5 (yellow) and Twist1 (red) (J).

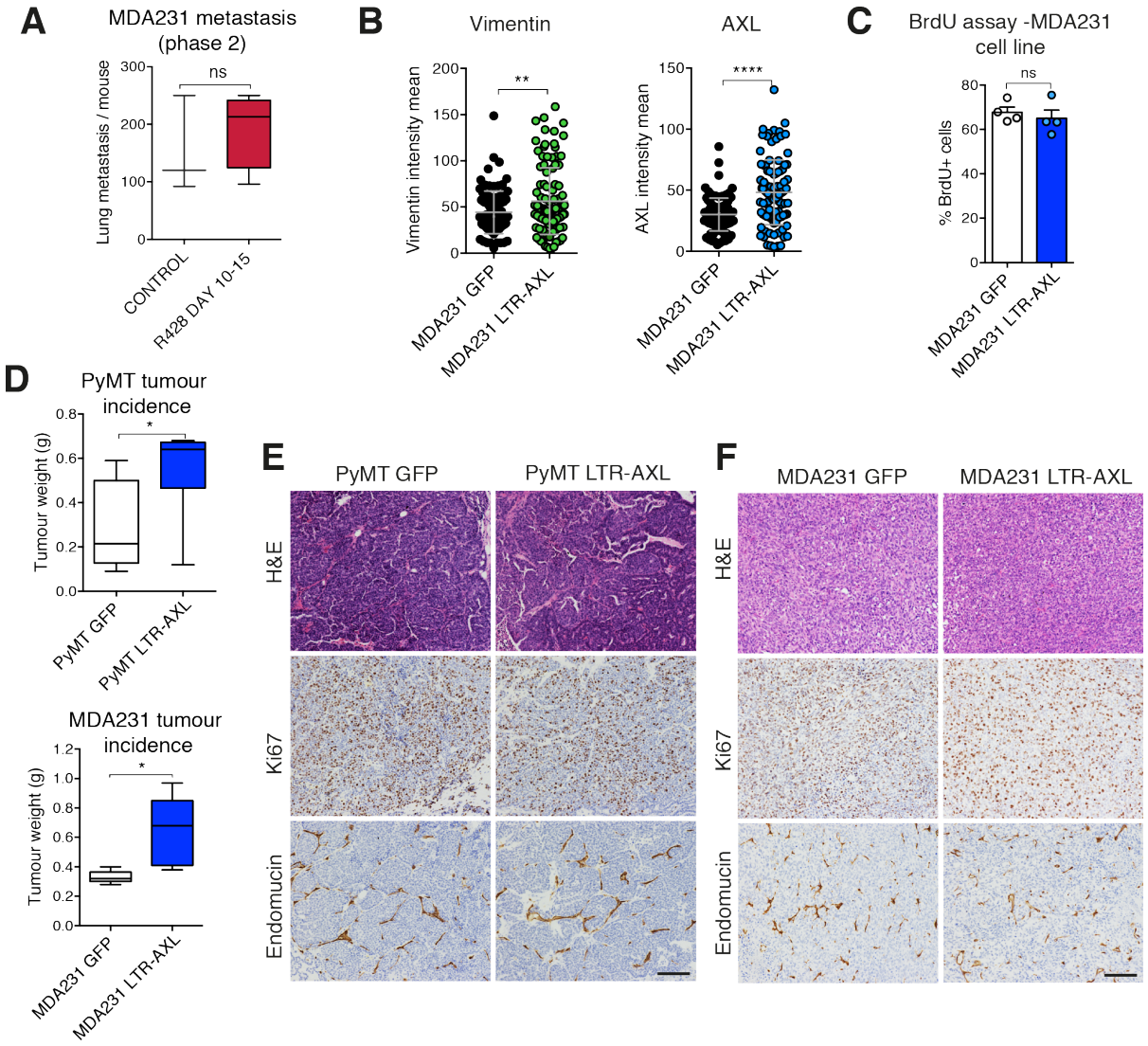

Figure S7 (relates to Figure 7). AXL exogenous expression in tumor cells

(A) Box plot displays the metastatic burden of MDA-MB-231 (MDA-231) cells intravenously injected into mice that were treated *in vivo* with DMSO or 12.5 mg/kg of R428 from day 10-15 post-injection (as described in Figure 7A). n= number of mice, CONTROL, 3; R428 (Day 10-15), 4. (B) Charts indicate the expression levels of Vimentin (left) and AXL (right) in MDA231 cells expressing GFP control or LTR-AXL constructs. Data from one representative experiment from two are shown. Line and error bar indicate mean ± SD of the population. (C) BrdU incorporation over a 3 hours pulse

by MDA231 cells expressing GFP control or LTR-AXL constructs. Histogram indicates mean ± sem of four independent experiments. (D) Box plots display the tumor burden assessed 2 weeks after engraftment of PyMT (upper panel) or MDA231 (lower panel) cells expressing GFP or LTR-AXL constructs (n=6 tumors per group). (E-F) Histological images of representative PyMT (E) or MDA231 (F) primary tumors expressing GFP or LTR-AXL constructs stained with Hematoxylin and Eosin, Ki67 or Endomucin. Scale bars, 100 µm.

- **Supplemental Tables**

Table S1. Mouse RT-PCR primers: relates to Figure S1D-F, S3B, S4H, S5I and S6C

GENE SYMBOL	Forward (5' – 3')	Reverse (3' – 5')
Gapdh	CGTGTTCCTACCCCCAATGT	TGTCATCATACTTGGCAGGTTTCT
Snai1	CTCTGAAGATGCACATCCGAA	GGCTTCTCACCAGTGTGGGT
Snai2	TGTGTCTGCAAGATCTGTGGC	TCCCCAGTGTGAGTTCTAATGTG
Twist1	GCCGGAGACCTAGATGTCATTG	CACGCCCTGATTCTTGTGAA
Zeb1	GCCAGCAGTCATGATGAAAA	TATCACAATACGGGCAGGTG
Myl9	AGGCCTCAGGCTTCATCCACGA	ATGGGGTCTAGGCACTGGGGC
Amotl2	AACCGCCACCTGGCAAGCAA	GGTCCTCGATGGCACCACGC
Ankrd1	AAACGGACGGCACTCCACCG	CGCTGTGCTGAGAAGCTTGTCTCT
Ccl2	CAGGTCCCTGTCATGCTTCT	GTCAGCACAGACCTCTCTCT
Ctgf	GCTTCGCAGGGCCTGACCAT	GCCGTGGGCTGCATTCCTCT
Icam1	GAAGCTTCTTTTGCTCTGCC	AGCAGTACTGGCACCAGAAT
Plac8	TCAGTGACTGCGGAGTCTGCC	CAGAGCTCTTGCCATCCAGCTCC
Spdr	GCCCAGCAGGTGCGCTATGA	CGGGGTGGCTTCCACGAGGT
Tagnl	AGGCGGCCTTTAAACCCCTCACC	CGGCCTACATCAGGGCCACAC
Thbs1	GCGTTGCCAGGCTCCGAGTT	GGTGCGCAGGCCCTTCAGTT
Angtl4	AAGATGCACAGCATCACAGG	ATGGATGGGAAATTGGAGC
Ccl7	AGCTACAGAAGGATCACCAG	CACATTCCTACAGACAGCTC
Ccl11	CAGATGCACCCTGAAAGCCATA	TGCTTTGTGGCATCCTGGAC
Cxcl10	GACGGTCCGCTGCAACTG	GCTTCCCTATGGCCCTCATT
Cyr61	GCCGTGGGCTGCATTCCTCT	GCGGTTCGGTGCCAAAGACAGG
Wnt5A	GGTGCCATGTCTTCCAAGTT	ATCACCATGCCAAAGACAGA
Col1A1[a]	TCGTGGCTTCTCTGGTCTC	CCGTTGAGTCCGTCTTTGC
Col4A1[a]	ATAGCCAAAGCCAAACCCATT	CGCAGAGCAGAAGCAAGAA
Lama2[a]	GTATCACCAAATTATCCAAGACCAT	TCGCTGGGCATATTTCTCATC
Fn1[a]	AAGAGGACGTTGCAGAGCTA	AGACACTGGAGACACTGACTAA

Mmp2[a]	GGACAAGAACCAGATCACATACA	GCCCGAGCAAAAGCATCAT
Mmp9[a]	TGATGCTATTGCTGAGATCCAG	CCTGTAATGGGCTTCCTCTATG
Mmp13[a]	CCAACCCTAAGCATCCCAAA	TCCTCGGAGACTGGTAATGG
Mmp14[a]	CCATCAATACTGCCTACGAGAG	CTCCTTAATGTGCTTGGGGTAC
Fscn1[a]	AAAGACTCCACGGGCAAGTA	GTCACAGAACTCAAGGAAGAAATC
Limkl[a]	TCTACAAGGACAAGCGGCTAA	CTCTGACTCCACGGGTACTG
Myhl10[a]	TCAGATGACGACACAGAAAGTAA	AGACTGGTGCTGGGATGAG
Pfn1[a]	ACCGTTCCCTTTGGCTTTTG	ATGTGGTTTTGGCAGCAATAAG
Mylk[a]	CCACCAGCACCATCACTCT	CCCAGGAGAGAAGGACCCTA
Thbs2[a]	GCCACCAGAACAACCAAGAC	CACCATCATTGTCATCATCAGAGT
Acta2[a]	CTCTTCCAGCCATCTTTCATTG	GTTGTTAGCATAGAGATCCTTCCT

[a] Design and validated by PrimerDesign Ltd, UK.

Table S2. Lentiviral plasmids description: relates to Supplemental Materials and Methods, 7.1. Lentiviral constructs generation

Name	Promoter /downstream sequence	Marker	Notes
GFP	LTR	hPGK-EGFP	Mild expression
LTRAXL	LTR-hAXLORF	hPGK-EGFP	Mild expression
shCONTROL	H1	hPGK-EGFP	High expression
shAXL	H1-mshAXL	hPGK-EGFP	High expression
shTHBS2 I	H1-mshTHBS2 I	hPGK-EGFP	High expression
shTHBS2 II	H1-mshTHBS2 II	hPGK-EGFP	High expression
VENUS	mPGK	hPGK-VENUS	High expression
THBS2ORF	mPGK-mTHBS2ORF	hPGK-VENUS	High expression

Table S3. shRNA sequences: relates to Supplemental Materials and Methods 7.1. Lentiviral constructs generation

shRNA	TARGET SEQUENCE (5' – 3')
shAXL F	GACATCTTCTTTCTCATGTGAAGCCCATCTGGTCATGGGCTTCACATGAGAAAGAAGATGTC TTTTT
shAXL R	AAAAAGACATCTTCTTTCTCATGTGAAGCCCATGACCAGATGGGCTTCACATGAGAAAGAAG ATGTC
shTHBS2 F	GCTGTAGGTTTCGACGAGTTTCTCGAGAAACTCGTCGAAACCTACAGCTTTTT
shTHBS2 R	AAAAAGCTGTAGGTTTCGACGAGTTTCTCGAGAAACTCGTCGAAACCTACAGC
shTHBS2 II F	CCACGTCAAGGACACTTCATTCTCGAGAATGAAGTGTCCTTGACGTGGTTTTT
shTHBS2 II R	AAAAACCACGTCAAGGACACTTCATTCTCGAGAATGAAGTGTCCTTGACGTGG

Table S4. Antibodies list: relates to Supplemental Materials and Methods 6.1. Histology; 10. Western blot; 11. BrdU assay; 13. Flow Cytometry and 14. Immunofluorescence

ANTIBODY	COMPANY	CATALOGUE No	CLONAL (CLONE)	DILUTION (TECHNIQUE)
Endomucin	Santa Cruz	sc-65495	Rat monoclonal (V.7C7)	1:200 (IHC-P)
Ki67 (human)	Dako	A047	Rabbit polyclonal	1:500 (IHC-P)
Ki67	Novocastra	NCL-Ki67p	Rabbit polyclonal	1:200 (IHC-P)
FAP-α	Santa Cruz	sc-54539	Goat polyclonal	1:100 (IF)
YAP	Santa Cruz	sc-101199	Mouse monoclonal (63.7)	1:50 (IF)
Vimentin (human)	Abcam	ab8978	Mouse monoclonal	1:100 (IF)
Vimentin	Sigma	V2258	Mouse monoclonal (LN-6)	1:200 (IF)
E-Cadherin	Abcam	ab11512	Rat monoclonal (DECMA-1)	1:200 (IF)
Twist1	Santa Cruz	sc-81417	Mouse monoclonal	1:50 (FC)
Zeb1	Santa Cruz	Sc-25388	Rabbit polyclonal	1:100 (IF)

AXL-biotinylated	R&D systems	BAF854	Goat polyclonal	1:100 (FC)
AXL	R&D systems	MAB8541	Rat polyclonal	1:100 (IF)
AXL (human)	R&D systems	MAB154	Mouse polyclonal	1:100 (IF/FC)
Integrin-β1 active	BD bioscience	550531	Rat monoclonal (9EG7)	1:50 (IF)
Integrin-β1	Abcam	ab24693	Mouse monoclonal (P5D2)	1:100 (B/IF)
CD24-AF450	eBioscience	48-0242-82	Rat monoclonal (M1/69)	1:100 (FC)
CD90-APC	eBioscience	17-0900-82	Mouse monoclonal (HIS51)	1:100 (FC)
SCA1-FITC	eBioscience	11-5981-82	Mouse monoclonal (D7)	1:100 (FC)
CD31-PE	eBioscience	12-0311-82	Rat monoclonal (390)	1:300 (FC)
CD45-PE	eBioscience	12-0451-82	Rat monoclonal (30-F11)	1:300 (FC)
Ter119-PE	eBioscience	12-5921-82	Rat monoclonal (Ter-120)	1:300 (FC)
FAK	Santa Cruz	sc-558	Rabbit polyclonal	1:300 (IF)
pFAK	Santa Cruz	sc-16563-R	Rabbit polyclonal	1:50 (IF)
ID1	Biocheck	BCH-1/195-14	Rabbit monoclonal (195-14)	1:100 (IF) / 1:5000 (WB)
pSMAD1-5	Cell signal	9511	Rabbit monoclonal (D5B10)	1:20 (FC)
pSMAD2-3	Cell signal	8828	Rabbit monoclonal (D27F4)	1:20 (FC)
BrdU	Abcam	ab6326	Rat monoclonal (BU1/75 ICR1)	1:100 (FC)
SMA-cy3	Sigma	C6198	Mouse monoclonal (1A4)	1:300 (IF)

- All antibodies are mouse specific, unless otherwise specified.
- IF: Immunofluorescence

- FC: Flow cytometry
- WB: Western Blot
- IHC-P: Immunohistochemistry – paraffin embedded tissue

- **Supplemental Experimental Procedures**

1. Statistical Analysis

Statistical analyses were performed using Prism software (GraphPad Software). P values were obtained from two-tailed Student t-tests with paired or unpaired adjustment. One column t-test was used for comparisons to a normalized value. One tail t-test was used for Figure 4E. Where indicated two-way ANOVA was used to perform multiple comparisons or multiple variables analysis between experimental groups. Significance was set at $p<0.05$. Graphs show the symbols describing p value (*, $p<0.05$; **, $p<0.01$; ***, $p<0.001$; ****, $p< 0.0001$).

2. Microarray samples and data analysis

.2.1 Accession Numbers

Microarray expression data were deposited in the Gene Expression Omnibus (GEO) database, available at http://www.ncbi.nlm.nih.gov/geo/. The accession number for the array data reported in this paper is GEO:GSE63558.

.2.2 Array samples preparation

MICs and nonMICs were freshly FACS sorted from late stage PyMT tumors according to their CD24-CD90 expression. RNA isolation was performed using MagMax-96 Total RNA Isolation Kit (AM1830, Ambion) that allows high quality RNA extraction from samples with low cell numbers, <10,000 cells. RNA quality for each sample was

assessed using Agilent RNA 6000 Pico Kit (5067-1511, Aligent Technologies) and only those samples with a RNA Integrity Number (RIN)>9 were considered for processing. RNA was amplified and analyzed on Illumina gene expression arrays (mouse) at the Barts and London Genome Centre.

.2.3 Gene expression data analysis

Gene expression data were analyzed by the Bioinformatics Unit at The Francis Crick Institute using Bioconductor version 2.2 available at http://bioconductor.org, running on R version 2.7.1 (R Core Team, 2013) available at http://www.R-project.org/. Normalized probe set expression values were calculated using log2 transformation and quantile normalization using the 'lumi' package (Du et al., 2008). To determine significant differences of expression levels between the different groups, a moderated Student's t test was computed on a probe-by-probe basis using the empirical Bayes statistics in the 'Limma' package (Smyth, 2005). The resultant p-values were adjusted for multiple testing using the False Discovery Rate (FDR) Benjamini and Hochberg method (Benjamini et al., 1995), where any probe sets that exhibited an adjusted p-value FDR $q<0.05$ were called differentially expressed.

Differentially expressed genes identified from MICs *versus* non-MICs (MIC signature) were used to generate a hierarchical Heatmap (Figure S1A). Genes were clustered using a Euclidean distance matrix and average linkage clustering. Red indicates higher expression and blue indicates lower expression relative to the mean expression of probes across the four samples.

Differentially expressed genes were used to determine enrichment of pathways and processes using MetaCore™ integrated software, version 6.19 developed by Thomson Reuters (2014), available at http://thomsonreuters.com/metacore/. This analysis employs a hypergeometric distribution to determine whether a list of differentially expressed genes is enriched in a pathway or process gene set relative to all genes on the array. Pathways or processes that showed a FDR of less than 0.05 were called enriched. The circos plot was generated plotting the top overexpressed pathways in MICs and a selection of their associated genes with reported roles in metastasis (Figure 1A).

.2.4 GSEA

The MIC signature was analyzed using the GSEA software developed by the Broad Institute of MIT and Harvard (USA) and available at www.broadinstitute.org, following the program guidelines to determine the correlation of specific published signatures with the MIC signature. The specific settings applied in all analyses are: number of permutations - 1,000, permutation type - gene set, enrichment statistic -weighted, metric for ranking genes - t-test. The rest of the fields were left as defaulted. The Wnt target genes signature was downloaded from the Wnt homepage Stanford University, available at http://web.stanford.edu/group/nusselab/cgi-bin/wnt/target_genes. The signature comprises a list of validated Wnt/β-catenin target genes. Farmer et al. previously published the TGF-β target genes and EMT signature (Farmer et al., 2009). Last, Dupont et al. published the YAP/TAZ signature (Dupont et al., 2011).

3. *In silico* data analysis

.3.1 cBioPortal for Cancer Genomics

The correlation analysis between the gene expression levels of *Thbs2* and different EMT markers was performed using cBioPortal for Cancer Genomics develop by Memorial Sloan Kettering Cancer Center (Cerami et al., 2012; Gao et al., 2013) and available at http://www.cbioportal.org/public-portal/. The tumor data set used was The Cancer Genome Atlas (TCGA provisional), Breast Invasive Carcinoma project (Cancer Genome Atlas, 2012).

.3.2 GOBO

Distant Metastasis-Free Survival (DMFS) prognosis prediction according to *Thbs2* gene expression levels and tumor grade in breast cancer patient data was done using GOBO (Gene expression-based Outcome for Breast cancer Online) 1.0.1 database developed by the Department of Oncology of Lund University and Skåne University Hospital (Lund, Sweden) and available at http://co.bmc.lu.se/gobo/. The tumor data set consists of 1881 samples (Ringner et al., 2011). All tumor types were selected for the analysis, splitting data in 3 quantiles and selecting 5 years for censoring data.

4. Quantitative real time PCR

For quantitative RT-PCR, RNA preparation was performed using either MagMax-96 Total RNA Isolation Kit (AM1830, Ambion) when RNA was isolated from less than 10^5 cells per sample, or RNeasy Mini Kit (QIAGEN) for higher cell numbers per sample.

cDNA synthesis was performed using and SuperScript III First-Strand Synthesis System (Invitrogen), according to the manufacturer's protocol.

Quantitative real-time PCR samples were prepared with 25ng total cDNA for each PCR reaction. The PCR, data collection and data analysis were performed on a 7500 FAST Real-Time PCR System (Life Technologies). The mouse primer pairs used for each of the mRNA targets are shown in Table S1.

5. Animal procedures

.5.1 Mouse strains

Transgenic FVB/n mice expressing the Polyoma Middle T-antigen (PyMT) oncogene under the Mouse Mammary Tumor Virus promoter (MMTV-PyMT) (Guy et al., 1992) were obtained from Dr Erik Sahai and used as sources of primary cancer cells. Cells were always isolated from late stage carcinomas.

RAG1 deficient FVB/n mice were obtained from Dr Joerg Huelsken. Age matched 6 to 10 weeks female were used as recipients for all orthotopic tumor transplantations and tail vein injections experiments, unless otherwise specified.

Nude (NuNu) CD1 mice were bought from Harlan UK and used for obtaining the samples for the microarray analysis. All the mice were kept in accordance with UK regulations under project license PPL 80/2531.

.5.2 Tumor initiation and metastatic colonisation assays

In tumor initiation assays (collective challenge), unless otherwise specified either $3x10^5$ PyMT primary cells or $1x10^6$ MDA-MB-231 cells were mixed in 100 µl of Growth Factor Reduced Matrigel (356230, Corning), and injected into the mammary fat pad of anesthetized mice. Tumor growth was evaluated 20 days after injection for early tumor initiation, and 6 weeks post-transplantation to evaluate differences in primary tumor growth and microenvironment.

For experimental metastasis assays (single cell challenge), unless otherwise stated, between $5x10^5$ – $1x10^6$ PyMT primary cells or $1x10^6$ MDA-MB-231 cells were resuspended in 100µl PBS and injected into the tail vein of mice. For metastatic assays where unlabeled PyMT and MDA-MB-231 cells were used, macrometastasis were evaluated either quantifying the number of superficial metastatic nodules using a Zeiss Lumar V.12 stereomicroscope or by histological analysis after Hematoxylin and Eosin (H&E) stain of lung sections. Other metastatic assays were performed using endogenously expressing, or lentivirus induced, GFP^+ or $Venus^+$ cells. Here metastasis were evaluated by quantifying the number of fluorescent metastatic nodules using Lumar V.12, (Zeiss), or by evaluating the percentage of GFP+ cancer cells in the lung by FACS analysis.

.5.3 Drug treatments

R428, also known as BGB324 (1946, Axon MedChem), was dissolved in DMSO at a final concentration of 21.15 mM or 12.5 mg/ml. *In vivo* treatments were performed as

previously described (Holland et al., 2010). Briefly, for the 24 hours treatment time point, PyMT cells were treated *in vitro* with either vehicle (DMSO) or 1.5 µM R428 for 3 hours, 24 hours before injection. The MDA-MB-231 cell line was pre-treated *in vitro* with 3 µM R428 for 3 hours, 24 hours before experiments were performed. For treatment during the first week of metastasis, cells were pre-treated in culture as described above, and after tail vein injection mice received a daily dose of 12.5 mg/kg R428 by oral administration. Treatments between 10-15, and 25-35 days post-injection were performed as described above, but cells were not pre-treated in culture before injecting them.

LDN193189 was dissolved in citric acid – sodium citrate buffer solution pH=3.1 at a final concentration of 6.25 mg/ml. Mice were injected with $1x10^6$ PyMT cells intravenously, and treated daily with an intraperitoneal (IP) dose of 35 mg/kg LDN193189 from day 5 to 12 post tumor cells IV injection.

6. Histology

.6.1 Lung immunofluorescence

Immunofluorescence to assess *in vivo* niche activation was performed in 4% PFA fixed, paraffin embedded lungs. 4 µm thick lung sections were cut, deparaffinised and rehydrated using standard methods. After antigen retrieval with citrate buffer, sections were stained with DAPI, an anti-GFP antibody to label tumor cells and either SMA to detect activated fibroblasts, or endomucin to detect endothelial cells (antibodies description and working concentrations in Table S4). Sections were mounted with Sudan Black B (SBS) to quench background auto-fluorescence.

Images were acquired in an upright Zeiss LSM780 confocal microscope. Quantitative analysis of images was performed manually counting the number of SMA^+ or $Endomucin^+$ cells in direct contact with the GFP-labeled tumor cells in the tissue.

.6.2 Immunohistochemistry (IHC-P)

Tumors were fixed in 4% PFA for 24h and then embedded in paraffin blocks. 4µm thick tumor sections were cut, deparaffinised and rehydrated using standard methods. After antigen retrieval, sections were stained with Hematoxylin and Eosin (H&E) solution, or alternatively with DAPI and antibodies against Endomucin (endothelial cells) and/or Ki67 (proliferating cells).

Images were acquired in an upright Nikon Eclipse Ni-U light microscope.

7. Lentivirus

.7.1 Lentiviral constructs generation

All lentiviral vectors used in this study were generated using Gateway® technology (Life Technologies).

The lentivirus constructs expressing short hairpin RNAs (shRNAs) were obtained in a two-step approach: first, the shRNA paired primers were designed with XhoI, BglII restriction sites on the edges to be cloned into a Gateway pENTR plasmid under the H1 promoter (attL1_H1promoter_cloning-site_attL2). Second, we performed a Gateway LR recombination between the pENTR plasmid containing the shRNA and the lentiviral vector p4300 (cPPT_CMVenh_attR_hPGK_EGFP_WPRE).

The lentiviral vectors expressing protein-coding DNA sequences were obtained by Gateway LR recombination between a pDONR plasmid containing the DNA coding sequence and a pDEST lentiviral backbone. For THBS2 overexpression, we engineered a lentiviral reporter construct excising the mouse *Thbs2* cDNA sequence with EcoRI (Addgene plasmid 12411; pcDNA3_mTSP2) and inserting it into a gateway pENTR. The generated pENTR was subsequently recombined with a pDEST lentiviral backbone that drives *Thbs2* gene expression under a mouse PGK promoter. The lentiviral backbone contains as well a truncated isoform of the human CD2 receptor (hCD2) and a Venus reporter gene. For a mild AXL expression, we recombined the pDONR plasmid containing the DNA coding sequence of *Axl* gene of human origin (Addgene plasmid 23945; pDONR223_AXLORF) with a pDEST lentiviral backbone that only has the lentivirus LTR driving regions and a CMV enhancer. The lentiviral backbone contains as well an EGFP reporter gene.

In Table S2 are the detailed descriptions of the expression constructs used in this study.

To generate the lentiviral vectors expressing shRNAs, we used hairpin oligomers with the target sequences shown in Table S3: 'shRNA sequences'. The shTHBS2 validated target sequences were taken from the website of Sigma Mission in collaboration with the RNAi consortium (TRC) scientist (http://www.sigmaaldrich.com/life-science/functional-genomics-and-rnai/shrna.html). The target sequence for shAXL was described previously (Gjerdrum et al., 2010). All these sequences do not match any cDNA sequence of the corresponding specie (mouse) registered in BLAST other than that of their own target gene.

.7.2 Lentivirus production

Third-generation VSV-G pseudo-typed high titre lenti-viruses were generated by transient co-transfection of 293T cells with a four-plasmid combination as follows: One 10 cm dish containing $1x10^6$ 293T cells was transfected using 2M $CaCl_2$, and 2x HBS (51558, Sigma) with 15 μg lentiviral vector, 6 μg pMD2-VSVG, 6 μg pRSV-rev and 6 μg pMDL-g/p-RRE. Fresh media was added 24h after transfection. Supernatants containing lentiviral particles were collected 48h and 72h hours after transfection, and concentrated by ultracentrifugation at 22,000 RPM.

.7.3 Primary cells lentiviral infections

For lentiviral transduction, 10^5 primary PyMT cells/well were seeded in 6-well tissue culture dish and infected with EGFP or Venus concentrated reporter lentiviruses added in suspension using 10 µg/ml Polybrene (107689, Sigma). After 48 hours cells were trypsinized and successfully transduced cells were FACS sorted according to their EGFP/Venus expression.

8. Cell culture

.8.1 Culture conditions and reagents

The human mammary carcinoma cell line MDA-MB-231 and the mouse carcinoma 4T1 cell line were obtained from the Cell services unit at The Francis Crick Institute, and maintained in standard 2D culture conditions in DMEM with 10% FCS at 37C and 5% CO_2.

Mouse mammary carcinoma primary PyMT cells were seeded 2D in plates coated with collagen-I coating solution (100 mg/ml BSA, 1M HEPES, 1:100 PureCol (5005-B, Advanced BioMatrix) in HBSS), and maintained in MEM media (DMEM/F12 supplemented with 2% FCS, 10µg/ml Insulin (I9278, Sigma), 20ng/ml EGF (PHG0313, Invitrogen) and 1:50 L-Glutamax (35050-061, Life Technologies), and grown at 37C and 5% CO_2 after isolation from late stage MMTV-PyMT derived carcinomas.

Mouse primary lung fibroblasts were isolated from a single-cell suspension of lung tissue that was depleted from $Ter119^+$ red blood cells, immune $CD45^+$ cells and endothelial $CD31^+$ cells by MACS sorting. The remaining fraction was cultured overnight on plastic in DMEM with 10% FCS. Unless otherwise specified, all fibroblast experiments were performed on cells seeded on the top of a thin layer of a 2:1 mixture of collagen I (354249; BD Biosciences) and Matrigel (354234; BD Biosciences) as described previously (Calvo et al., 2013).

Fibroblast cell lines where obtained from the Sahai Laboratory. For generating the NLF3 cell line, normal lung fibroblasts were isolated from healthy lungs of aGFP/FVB/n mice. Lung CAFs were isolated from metastatic lungs of MMTV-PyMT FVB/n mice, and the mCherry CAFs were isolated from primary MMTV-PyMT FVB/n tumors in carcinoma stage. All fibroblast cell lines were generated according to the published Bio-protocol e1097 (Calvo, F., Hooper, S. and Sahai, E. (2014). Isolation and Immortalization of Fibroblasts from Different Tumoral Stages. Bio-protocol 4(7): e1097), available at http://www.bio-protocol.org/e1097. Briefly, tissue pieces are placed into dishes where

they are compressed under a 20 mm coverslip in DMEM media under sterile conditions. After 7 days, fibroblasts have come out of the tissue into the coverslip and the dish and can be trypsinased with Trypsin/EDTA and transferred into a new dish. Once they reach 80% confluency, primary fibroblasts are immortalized by infection with pBABE-HPV-E6-puromycin retroviruses. Positively infected fibroblasts are selected by addition of puromycin (2 μg/ml final concentration) in the complete culture media for 7-10 days, when resistant clones expressing HPV-E6 (i.e. immortalized cell lines) are visible.

.8.2 *In vitro* drug treatments

R428 (1946, Axon MedChem) *in vitro* treatment was performed as previously described (Holland et al., 2010). Briefly, PyMT primary cells plated 2D were treated with either vehicle (DMSO) or 1.5 µM R428 for 3 hours before washing and adding fresh media. 24 hours after *in vitro* assays were performed. MDA231 cells were treated with 3 µM R428. Next day *in vitro* assays were performed.

LDN193189 was dissolved in DMSO to 10 mM and use at a final concentration of 1 µM in the cell culture media. A single treatment was used as experiments were done over 24 - 48h.

.8.3 CAF-conditioned media

To assess the effects of CAF-derived soluble factors on tumor cells with the specific BMP inhibitor LDN193189 (Figure 6L-M), CAFs were plated to reach confluency the day

after in fresh DMEM with 10% FCS (as described in the 8.1). DMEM with 10% FCS, or 24h CAF conditioned media was collected and concentrated 4x using Millipore Centriprep® 10K Centrifugal Filter Concentrators (Millipore, MIL4304). The concentrated media was used to treat PyMT tumor cells plated in collagen-I coated dishes for 24h, supplemented with 1μm LDN193189 and then either western blot analysis or immunofluorescence for ID1 was performed (antibody details and working concentration can be found in Table S4).

9. Tumor sphere assay

Cells prepared as a single-cell suspension were plated in Ultra Low Attachment 96-well plates (Constar) with Sphere Media (DMEM/F12 supplemented with 1:50 B27 (Invitrogen), 20ng/ml EGF (PHG0313, Invitrogen), 20ng/ml FGF (PHG0026, Invitrogen), 4mg/ml heparin (H3393, Sigma)), and kept at 37C and 5% CO_2.

PyMT primary cell spheres were established from total tumor cell preparations. After tumor dissociation, cells were plated on collagen overnight; trypsinazed and 10^4 cells/ 200ul per well were seeded. Only the characteristic hollow spheres formed by these cells were quantified as tumor-spheres.

For passaging, tumor-spheres were collected by centrifugation and dissociated both enzymatically by trypsin treatment (for 10 min at 37 °C) and mechanically by using 25G needles, and the resulting single-cell suspension was counted and re-plated at the original density.

Quantitative analysis of images was performed using ImageJ software, and the Sphere Formation Index (SFI) was calculated considering both, number and size of the spheres,

and was obtained by summing the area of all spheres formed divided by the number of single cells initially plated.

10. Western blotting

$CD24^{+}AXL^{+}$ cells were FACS sorted and cultured in collagen-I coated dishes overnight (as in 8.1) and incubated for 24h with the pertinent media and treatments. Protein lysates were obtained after cell lysis with RIPA buffer (50mM Tris-HCl, 1% NP-40, 0.5% Na-deoxycholate, 0.1% SDS, 150 mM NaCl, 2 mM EDTA, 50 mM NaF) supplemented with Roche cOmplete protease inhibitors cocktail tablets following standard procedures. Protein lysates were run in 12% polyacrylamide gels and blotted into Amersham™ Polyvinyllidine difluoride membranes (10-6000-29). Membranes blocking and antibody staining were performed in 5% BSA/PBS. Antibody description and working concentration used can be found in Table S4.

11. BrdU proliferation assay

Cancer cells proliferation rate was assessed measuring their nuclear BrdU incorporation after culturing them for 3 hours in 30 μM BrdU supplemented media (as in 8.1). Then, cells were washed with PBS, trypsinazed, fixed with 70% ethanol for 20 mins, permeabilized with 2N HCl, 0.5% TritonX-100 for 30 mins, and treated with 0.1M tetraboric acid for 2 mins. After washing twice with FACS buffer and cells were stained with anti-BrdU antibody (Table S4).

12. ELISA

To measured THBS2 secretion, tumor cells were plated in adherent conditions (as in 8.1) at a cell density of 50,000 cells per 100 µl. The resulting conditioned-culture media was collected 24h after plating and frozen at -80C.

To quantify the levels of secreted protein in the conditioned-media, we used two different sandwich-ELISA kits, THBS2 ELISA Kit (SED822Mu, Cloud-Clone Corp) and Mouse THBS2 ELISA Kit (MBS942662, MyBioSource), and proceed according to the manufacturer's protocols. The resulting colorimetric reaction was measured at 450nm using an automated ELISA plate reader (SpectreMax 190 Microplate Reader, Molecular Devices).

13. Flow cytometry

.13.1 FACS analysis

Flow cytometry analyses were carried out on a BD LSR-Fortessa system (BD Biosciences), and Propidium Iodide (PI) was used as a viability dye unless otherwise indicated.

To examine the relationship between MICs, AXL and SCA1 in primary PyMT cells, PyMT tumors were dissociated and plated overnight on collagen-I coated dishes. Next day, cells were trypsinazed and stained for CD24 as an epithelial marker in combination with SCA1, AXL and CD90 in MACS buffer (0.5% BSA and 1mM EDTA in PBS). Antibody description and working dilutions can be found in Table S4.

To assess AXL expression in metastatic lungs containing GFP labeled cancer cells, the tissue was dissociated and prepared as a single cell suspension as previously described (Malanchi et al., 2012). Subsequently, it was stained for lineage negative markers (CD31, CD45 and Ter119), CD24, CD90 (when expression was targeted to MICs) and mAXL-biotin or hAXL in MACS buffer. Antibody description and working dilutions can be found in Table S4.

The expression of different protein assessed by FACS in MDA231 cell line was done after trypsinization of cultured cells (as in 8.1) and staining with the pertinent antibodies in MACS buffer.

Differences in extravasation to the lungs by R428-treated or untreated PyMT cells was assessed by perfusing the lungs with PBS to flush out the blood, and then the clean tissue was dissociated in single-cell suspension and the number of GFP^+ MICs or nonMICs (according to CD24/CD90 expression as in 13.1) present in the lungs were quantified.

.13.2 Cell sorting

All cell-sorting experiments were carried out on either a BD Influx or FACSAria cell sorter systems (BD bioscience).

To sort the MICs from PyMT primary tumors or lungs containing GFP labeled cancer cells we used the staining indicated above (13.1). $CD24^+AXL^+$ and $CD24^+AXL^-$ cells were sorted from primary PyMT tumor single-cell preparations plated overnight. The staining protocol previously described (Malanchi et al., 2011), was adapted and a mAXL-

biotinylated antibody was incorporated and conjugated to streptavidine-PEcy7 (Life Bioscience, 25-4317-82) (antibody description and working dilutions can be found in Table S4).

EGFP^{+} or Venus^{+} cells expressing the lentiviral constructs were trypsinazed, washed with MACS buffer and sort according to the expression of the reporter gene.

.13.3 ImageStream analysis

Image stream analyses were carried out in an ImageStream®^{X} Mark II Imaging Flow Cytometer (Amnis-Millipore).

For whole lung analysis, cells were dissociated into a single cells suspension and depleted by MACS sorting from lineage negative cells (Ter119, CD45 and CD31). Next, the remaining fraction was stained with a live/dead fixable Near-Infrared dye (Invitrogen, L10119) and after fixed with 2% PFA for 30 mins and permeabilized with 0.1% Trinton-X for 10 mins. Next, cells were resuspended in FACS buffer (2% FCS in PBS) and stained with primary antibodies against Twist1, pSMAD1-5, ID1 or pSMAD2-3 at 4C overnight (antibody description and working dilutions can be found in Table S4). Subsequently, cells were washed twice in MACs buffer (0.5% BSA and 1mM EDTA in PBS) and incubated for 45 mins with secondary antibodies at room temperature. DAPI was added at 0.5 µg/ml to cells before analysis for nuclear staining. Tumor cells were identified by GFP expression.

In vitro, ImageStream analysis of non-labeled MICs co-cultured with NLF3 for 4-5 days (as specified in the scheme in Figure 2E) was performed from a single cell suspension after gel digestion. NLF3 were excluded by GFP expression, and MICS were analyzed for Twist1 expression changes (Figure 6D-E).

The acquired data was analyzed using Amnis IDEA management software to compensate for multi-color spectral overlap; plot and graphical gating of the cells as well as obtaining representative images of cells.

14. Immunofluorescence

All cancer cell immunofluorescence microscopy was performed on cells seeded on glass-bottom 35 mm MatTek dish (P35-1.5-14-C, MatTek) or glass coverslips coated (Thermo Scientific) with collagen solution (Cell culture procedure). Samples were fixed with 4% PFA for 10 min, permeabilized with 0.5% TritonX-100 for 30 min and 0.1% TritonX-100 for 20 min. Samples were blocked for 45 min at room temperature in blocking solution: 4% BSA in PBS with 0.05% Tween20 (Sigma). Then, cells were incubated with primary antibody in blocking solution overnight at 4 C. After 3 washes of 5 min in PBS, secondary antibody in blocking solution was added. After 3 washes of 5 min in PBS, samples were mounted using Dako Fluorescent Mounting Media (S3023, Dako), and analyzed using either upright or inverted Zeiss LSM710.

Quantitative analysis of images was performed using Imaris 7.6.4. Tumor cells were identified using an automated threshold based on GFP expression or a homogenous cell body staining. The mean intensity of E-Cadherin, AXL and Vimentin was then measured.

All fibroblast immunofluorescence, unless stated otherwise, were performed on cells seeded on the top of a thin layer of a mixture of 2:1 collagen-I:Matrigel as described previously (Calvo et al., 2013). Briefly, after 24h on the gel and the pertinent treatments, cells were fixed in 4% paraformaldehyde for 1 h. Cells were permeabilized by incubation in PBS 0.5% NP-40 (Sigma) at 4C for 20 min, in PBS with 0.3% Triton X-100 (Sigma) at room temperature for 20 min and in PBS with 0.1% Triton X-100 at room temperature for 15 min. Samples were blocked for 60 min at room temperature in blocking solution: 4% BSA in PBS with 0.05% Tween20 (Sigma). Then, cells were incubated with primary antibody in blocking solution in a wet chamber overnight at 4C. After 3 washes of 15 min in PBS, secondary antibody in blocking solution was added. After 3 washes of 15 min in PBS, samples were mounted and analyzed using an inverted Zeiss LSM710.
Quantitative analysis of images of CAF markers was performed using Imaris 7.6.4. To quantify FAP, fibroblasts were identified using an automated threshold based on their GFP expression. The mean intensity of FAP was then measured.

Antibody description and working dilutions can be found in Table S4.

15. Live cell imaging

For two dimensional image acquisition cells were plated sub-confluent into 24-well glass bottom MatTek plates (P24G-1.5-10F, MatTek) coated with collagen solution. Once attached, cells were kept in the microscope chamber at 37C and 5% CO_2 and images were acquired every 5 mins for 12 hours. The acquired digital images were merged

using MetaMorph Automation and Imaging Analysis Software (Molecular Devices Inc.). Cell tracking speed analysis was performed using Mathematica 8.0 (Wolfram).

16. Fibroblasts and tumor cells co-cultures

Experimental set up 1 (Figure 2E). To assess fibroblast activation via the induction of different activation markers over 24h, GFP labeled NLF3 cells were seeded on top of a layer of 2:1 collagen-I:Matrigel mix in a 35-mm glass-bottom MatTek dish (P35-1.5-14-C, MatTek), together with tumor cells in a 1:3 fibroblast:tumor cells ratio. Normally on 100 µl of gel mix, $1.5x10^4$ GFP NLF3 cells were seeded with $4.5x10^4$ sorted MICs/nonMICs. The co-culture was maintained in MEM media (DMEM/F12 supplemented with 2% FCS, 10µg/ml Insulin (I9278, Sigma), 20ng/ml EGF (PHG0313, Invitrogen) and 1:50 L-Glutamax (35050-061, Life Technologies).

The same experimental setting was used to evaluate the impact of activated NLF3 on MICs mesenchymal inhibition (Figure 6D-E). In this case, to ensure NLF3 full activation the co-cultures were incubated 3-5 days before analysis, and tumor cells were examined by flow cytometry for AXL expression or by ImageStream for Twist1 expression.

Experimental set up 2 (Figure 2I): To assess fibroblast activation via their ability to remodel an extracellular matrix, normal primary lung fibroblasts or the NLF3 cell line were embedded in 100 µl of 2:1 collagen-I:Matrigel and seeded on a 35-mm glass-bottom MatTek dish (P35-1.5-14-C, MatTek). Once the gel was set, we introduced a low height co-culture insert (PICM-ORG-50, Millipore) where tumor cells were seeded in a

1:3 fibroblast:tumor cells ratio. The co-culture was maintained in MEM media (DMEM/F12 supplemented with 2% FCS, 10µg/ml Insulin (I9278, Sigma), 20ng/ml EGF (PHG0313, Invitrogen) and 1:50 L-Glutamax (35050-061, Life Technologies). Unless stated otherwise, the gel contraction value refers to the contraction observed after 3 days, obtained by comparing the relative diameters of the well and the gel using ImageJ software, and the contraction was calculated as the gel area relative to the well area in arbitrary units (A.U.).

Experimental set up 3 (Figure S6D): To assess the effect of fully converted CAFs over the phenotypic mesenchymal features of cancer cells, sorted MICs were plated overnight in collagen-I coated 35-mm glass-bottom MatTek dish (P35-1.5-14-C, MatTek). Next day, we introduced a low height co-culture insert (PICM-ORG-50, Millipore) were CAFs were seeded in a 3:1 fibroblast:tumor cells ratio for 24h. The co-culture was maintained in MEM media (DMEM/F12 supplemented with 2% FCS, 10µg/ml Insulin (I9278, Sigma), 20ng/ml EGF (PHG0313, Invitrogen) and 1:50 L-Glutamax (35050-061, Life Technologies).

17. 3D spheroids assays

.17.1 Mixed spheroids invasion assay

GFP^+ MICs were freshly isolated from an actin-GFP MMTV-PyMT mouse and GFP^- nonMICs were isolated from unlabeled MMTV-PyMT mice by cell sorting according to their CD24/CD90 expression (see 13.1).

Next, GFP^+ MICs and GFP^- nonMICs were re-aggregated in ultra-low attachment conditions overnight in 1:9 ratio, in line with their relative distribution in primary tumors *in vivo*. The micro-spheroids formed were embedded in: pure collagen-I BD Biosciences cat. no. 354249), a 2:1 mixture of collagen-I and Matrigel (BD Biosciences cat. no. 354234), yielding a final collagen-I concentration of ~4.6 mg/ml and a final Matrigel concentration of ~2.2 mg/ml. Micro-spheroids were allowed to invade for 48 hours before fixation with 4% PFA and staining with Phalloidin-TRITC (Sigma P-1951) and DAPI. Spheroids were imaged using a Zeiss LSM780 confocal microscope and invasive cells quantified using Volocity 3D Image Analysis Software by PerkinElmer.

.17.2 Spheroids-CAFs invasion assay

FACS sorted GFP^+ MICs or nonMICs were re-suspended in DMEM with 10% FBS and 0.2% methyl cellulose at 2.5 x 10^5 cells/ml with or without 2.5 x 10^4 mCherry labeled PyMT-CAF. Spheroids were formed by hanging drop assay overnight and then embedded in 2:1 collagen-I:Matrigel mix. Spheroids were allowed to invade for 48 hours before fixation with 4% PFA, followed by DAPI staining. Spheroids were imaged using a Zeiss LSM780 confocal microscope and invasive cells quantified using Volocity 3D Image Analysis Software by PerkinElmer.

.17.3 Organoid assay in Matrigel

A single cell suspension of FACS sorted MICs was pre-treated with R428 (as specified in 8.2) and then directly seeded in pure Matrigel and maintain in Sphere Media

(DMEM/F12 supplemented with 1:50 B27 (Invitrogen), 20ng/ml EGF (PHG0313, Invitrogen), 20ng/ml FGF (PHG0026, Invitrogen), 4mg/ml heparin (H3393, Sigma)) at 37C and 5% CO_2 for 10 days. After 3 days cells are grouped into clusters. Quantitative analysis of images was performed 10 days after seeding using ImageJ software. The Organoids Formation Index (OFI) was determined considering both, number and size of the organoids, and was obtained by summing the area of all organoids formed divided by the number of single cells initially plated.

- **Supplemental References**

Cancer Genome Atlas, N. (2012). Comprehensive molecular portraits of human breast tumours. Nature *490*, 61-70.

Cerami, E., Gao, J., Dogrusoz, U., Gross, B.E., Sumer, S.O., Aksoy, B.A., Jacobsen, A., Byrne, C.J., Heuer, M.L., Larsson, E.*, et al.* (2012). The cBio cancer genomics portal: an open platform for exploring multidimensional cancer genomics data. Cancer discovery *2*, 401-404.

Du, P., Kibbe, W.A., and Lin, S.M. (2008). lumi: a pipeline for processing Illumina microarray. Bioinformatics *24*, 1547-1548.

Dupont, S., Morsut, L., Aragona, M., Enzo, E., Giulitti, S., Cordenonsi, M., Zanconato, F., Le Digabel, J., Forcato, M., Bicciato, S.*, et al.* (2011). Role of YAP/TAZ in mechanotransduction. Nature *474*, 179-183.

Farmer, P., Bonnefoi, H., Anderle, P., Cameron, D., Wirapati, P., Becette, V., Andre, S., Piccart, M., Campone, M., Brain, E.*, et al.* (2009). A stroma-related gene signature predicts resistance to neoadjuvant chemotherapy in breast cancer. Nat Med *15*, 68-74.

Gao, J., Aksoy, B.A., Dogrusoz, U., Dresdner, G., Gross, B., Sumer, S.O., Sun, Y., Jacobsen, A., Sinha, R., Larsson, E.*, et al.* (2013). Integrative analysis of complex cancer genomics and clinical profiles using the cBioPortal. Sci Signal *6*, pl1.

Guy, C.T., Cardiff, R.D., and Muller, W.J. (1992). Induction of mammary tumors by expression of polyomavirus middle T oncogene: a transgenic mouse model for metastatic disease. Mol Cell Biol *12*, 954-961.

Ringner, M., Fredlund, E., Hakkinen, J., Borg, A., and Staaf, J. (2011). GOBO: gene expression-based outcome for breast cancer online. PLoS One *6*, e17911.